JOURNAL OF COMPUTATIONAL PHYSICS 34, 1–53 (1980)

Review

The Accuracy, Efficiency, and Stability of Three Numerical Models with Application to Open Ocean Problems

D. B. HAIDVOGEL,* A. R. ROBINSON, AND E. E. SCHULMAN

Division of Applied Sciences, Harvard University, Cambridge, Massachusetts 02138

Received December 4, 1978; revised May 15, 1979

The inviscid barotropic vorticity equation is integrated under a variety of assumed initial and boundary conditions corresponding to linear and nonlinear box modes, forced nonlinear box modes, and linear and nonlinear Rossby waves (with and without mean advection). The former two classes of problems are defined within a closed domain. The latter is partially or totally open to a specified external environment and therefore represents prototype limited-area calculations for the ocean. To determine the extent to which the accuracy and efficiency of limited-area calculations depend on the numerical integration scheme, each test problem is solved independently using the finite-difference (FD), finite-element (FE), and pseudospectral (PS) techniques. The three numerical models differ primarily in the formal accuracy of their spatial approximations and their treatment of vorticity at outflow points along the boundary. The *FD* model employs a centered second-order differencing scheme and requires an extrapolatory (computational) boundary condition to fix the values of vorticity at outflow boundary points. The *FE* model, which represents ψ and ζ as a summation of piecewise linear elements, is of fourth order for the linearized one-dimensional advective equation. Further, a technique is developed by which the determination of the interior values of ζ is decoupled from that of the boundary values; hence, the vorticity boundary conditions can be implemented without iterative techniques. Lastly, the "infinite-order" PS model avoids the assumption of lateral periodicity by expanding ψ and ζ in a double series of Chebyshev polynomials. The resulting vorticity equation is solved in the spectral domain using a modified alternating direction implicit method. All three models are of second order in time and have conservative formulations of the nonlinear terms. Integrations of moderate length (5–10 periods of the known analytic solution) are performed to determine the accuracy, stability, and efficiency of each model as a function of problem class and the associated physical and computational nondimensional parameters. The most important of these parameters are ϵ, the Rossby number; ν, the number of spatial degrees of freedom (grid points, expansion functions, etc.) per half wavelength of the reference solution; and η, the number of time steps per period of the reference solution. The latter two parameters are nondimensional measures of the spatial and temporal resolution of the numerical approximation. These tests show that all three models are, in general, capable of delivering stable and efficient solutions to linear and weakly nonlinear problems in open domains ($0 \leqslant \epsilon \leqslant 0.4$, $4 \leqslant \nu \leqslant 10$, $64 \leqslant \eta \leqslant 128$). Despite their added complexity, however, the FE and PS models are on the average, 4 and 15 times more accurate, respectively, than the FD model even taking into account its increased efficiency. The results also suggest that given a judicious selection of a frictional (filtering) mechanism and/or computational boundary condition (to suppress the accumulation of grid-scale features), each of the models can be made similarly accurate for highly nonlinear calculations ($\epsilon \geqslant 0.4$).

* Present address: Clark Laboratory, Woods Hole Oceanographic Institution, Woods Hole, Mass. 02543.

0021-9991/80/010001 53$02.00/0

1. Introduction

Limited-area modeling of the oceans is important for both scientific and (potentially) practical problems including (1) simulations of geographically and/or dynamically distinct subregions of the ocean, and (2) idealized dynamical studies of oceanic processes and models [1]. Examples of the first kind or regional problems are limited-area ocean forecasting [2], coastal modeling [3], and the simulation of intense current systems and their associated instabilities [4]. Studies of the second kind are useful for the determination of the dependence of regional dynamic balances on specific model parameters including environmental factors, as have been done with eddy-resolving simulations of the general circulation of entire ocean basins [5]. For limited-area ocean problems, the effects of changes in the externally imposed bounding conditions can also be addressed in the form of idealized modeling studies. Both categories of limited-area problems relate in a significant way to ongoing and anticipated field measurements from a variety of modern techniques including novel four-dimensional synoptic data sets (i.e., deep ocean regional weather maps) [6–8] and satellite surveys of the upper ocean [9].

The general circulation of the ocean and its variability are known to be made up of different regions of different dynamical characteristics [10]. For an oceanic regime which is spatially statistically homogeneous, local dynamic studies can be made with periodic boundary condition models. Such models assume that the physics is locally determined and essentially independent of information such as scales and amplitudes which could be generated elsewhere and continuously transported across the boundaries. Such "process" models have been used to investigate the dynamical properties of the mesoscale eddy field under simulated midocean conditions in regions assumed to be well removed from boundary influences [11, 12]. As has become increasingly clear both from the empirical data base as well as a growing number of mesoscale-resolution ocean circulation studies, the most interesting subregions are inhomogeneous [5]. For such regions (examples of which have been given above), as well as for many other limited-area hydrodynamic problems, other more complicated boundary conditions are necessary.

The determination of valid and convenient forms of boundary conditions, particularly at points of outflow, constitutes a major, essentially unresolved, problem in the modeling of many hydrodynamic systems over regional domains. The choice of boundary conditions involves a number of physical, mathematical, and numerical (or computational) considerations. On large and regional scales, the conditions should correctly represent or parameterize the interaction of the (arbitrary) volume of fluid with its surroundings. Smaller scale physical phenomena generated internally within the region should not be trapped but allowed to pass out of the domain; i.e., the model boundary should be transparent for such small-scale processes. The mathematical problem consisting of model equations and boundary conditions should be well posed in some reasonable sense; e.g., as defined by Oliger and Sundstrom [13]. The numerical scheme chosen for computational purposes should be of desired accuracy and acceptable efficiency.

In its discrete (computational) form, a given numerical model may involve the use of boundary information which is not in principle required in the well-posed analytical problem. Such auxiliary information is known as a computational boundary condition and should be chosen for convenience and efficiency, but should not in principle affect physical results. In practice, specific problems appear to require special conditions and a trial and error approach is usually indicated. Alternate choices of boundary conditions do, however, affect the accuracy and stability of regional computations; illustrative examples are given below.

In this paper we evaluate the feasibility of performing idealized open ocean calculations, using as a physical model the vorticity equation for barotropic (i.e., depth-independent) flow in an inviscid ocean of constant depth. In an early and pioneering atmospheric forecasting study, Charney, Fjortoft, and von Neumann [14] originally argued heuristically that consistent solutions to the inviscid barotropic vorticity equation could be obtained by specifying values of the streamfunction at all boundary points, and values of vorticity at only inflow points. Sundstrom [15] claims to have established the well-posedness of the analytic Charney-Fjortoft-von Neumann problem. This result has been questioned recently, however, by Bennet and Kloeden [16], who suggest that the smoothness of solutions to the barotropic vorticity equation subject to inflow boundary conditions is in doubt due to the necessary occurrence of points on the boundary where the flow is tangential.

Unless iterative or implicit numerical techniques or one-sided differencing schemes are used, inviscid calculations with the discrete barotropic vorticity equation require some auxiliary relationship to prescribe vorticity at outflow boundary points. Several types of boundary conditions have been used in attempts to avoid problems associated with outflow, including extrapolatory formulas [15, 17] and radiation conditions [18, 19]. For systems—such as that investigated here—which admit dispersive wave solutions, appropriate forms of such boundary conditions are difficult to determine and often quite complex [20]. In addition, the resulting numerical scheme is often sensitive to the specific choice of computational boundary condition. The original calculations made by Charney, Fjortoft, and von Neumann [14], for instance, were weakly unstable due to their choice of computational boundary condition. In another example, Shapiro and O'Brien [21] have also shown that, while the method of characteristics works well as a computational boundary condition, specification of known or presumed values of vorticity at outflow boundary points may lead to numerical instability.

Keeping in mind these potential areas of complication, we have attempted to explore the possibility of barotropic regional ocean modeling by investigating and comparing the accuracy, efficiency, and stability of three limited-area numerical models based, respectively, on the finite-difference, finite-element, and spectral approximation methods [22]. The physical boundary conditions used are the Charney–Fjortoft–von Neumann conditions. The calculations are mostly inviscid but in some cases a dissipative filter is included. The three codes differ substantially in the details and formal accuracy of their spatial discretization schemes and in their treatment of the vorticity at outflow. It should therefore be stressed at the outset that these models

have *not* been chosen to provide an unbiased intercomparison of finite-difference, finite-element, and pseudospectral techniques in general. Our intent rather has been to investigate a range of computational approaches representing both traditional and somewhat more novel numerical methods and to choose that model most suited to our limited-area modeling needs. It could not be anticipated beforehand, for instance, how easily and efficiently the higher-order finite-element and pseudospectral schemes could be adapted to regional modeling applications. The statement of the nondimensional vorticity equation and a description of the numerical techniques are given in Sections 2 and 3.

The three models have been tested and intercompared for a variety of prototype physical problems in closed and open basins and over a range of the nondimensional physical and computational parameters corresponding to each problem class. First, the unforced (homogeneous) solutions to the linear and nonlinear vorticity equation in a closed basin are found and compared to the known exact and perturbation solutions for linear and nonlinear box modes, respectively (Section 4). With the addition of a body force, various exact nonlinear closed-basin solutions are constructed and tested (Section 5). In an infinite domain, linear and nonlinear Rossby wave solutions are well known to be possible. These are dispersive planetary waves, whose existence depends on the restoring force provided by the earth's rotation. Limited-area open domain Rossby wave solutions are obtained, discussed, and intercompared in Section 6.

Model–model intercomparisons of this type have been carried out for simple advective problems in closed basins (e.g., Orszag and Israeli [22]). To our knowledge, however, this is the first such study that encompasses limited-area hydrodynamic modeling problems as well. Following the recent acquisition of a reliable midocean synoptic data base [6], one of the three models to be discussed (the finite-element) has now been applied to a series of barotropic regional forecast studies. Preliminary test results have been reported elsewhere [23, 24].

2. Modeling Equations, Methodology, and Format of Results

We consider the barotropic vorticity equation on a β-plane, which can be written in dimensional form as

$$\left\{\frac{\partial}{\partial t} + J(\psi, \ )\right\}(\zeta + f) = F(x, y), \qquad 0 \leqslant x \leqslant L_x, \quad 0 \leqslant y \leqslant L_y, \tag{1}$$

where

$$f = f_0 + \beta y$$

and

$$J(\psi, \ ) = \frac{\partial \psi}{\partial x}\frac{\partial}{\partial y} - \frac{\partial \psi}{\partial y}\frac{\partial}{\partial x}.$$

In addition,

$$\zeta = \nabla^2\psi \tag{2}$$

is the relationship between streamfunction (ψ) and vorticity (ζ), and $F(x, y)$ represents the effects of a body force, if any. Dissipation has been neglected for three reasons. First, the inviscid system poses a simpler physical and numerical problem, one for which many analytic and perturbation solutions are available. This is the basis of our testing of the limited-area models described in Section 3. Second, quadratic conservation laws are available for nondissipative physical and numerical systems. This property also contributes to the evaluation of model performance. Lastly, by ignoring explicit higher-order friction, we sidestep for the moment the question of the correct specification of vorticity boundary conditions on outflow, which are not formally needed for integration of the inviscid system. The assumption of inviscid dynamics does, however, require that greater care be taken to construct a numerical scheme which is stable in the absence of explicit dissipative (that is, smoothing) mechanisms. As we shall see, such filtering is in fact necessary to maintain stability in some cases.

If we now nondimensionalize x, y, t, and ψ by d, d, $(\beta d)^{-1}$, and $(V_0 d)$, respectively, then (1) becomes, in nondimensional form,

$$\left\{\frac{\partial}{\partial t} + \epsilon J(\psi, \ )\right\} \nabla^2\psi + \psi_x = F(x, y), \qquad 0 \leqslant x \leqslant x_B, \quad 0 \leqslant y \leqslant y_B, \tag{3}$$

where the Rossby number

$$\epsilon = V_0/\beta d^2$$

and

$$x_B = L_x/d, \qquad y_B = L_y/d.$$

The parameters d and V_0 are taken to be the characteristic length and velocity scales of the anticipated field of motion. Note that the length scale d does not correspond to the basin dimensions L_x or L_y; hence, x_B and y_B are, in general, greater than one.

The modeling strategy developed herein involves the integration of Eq. (3) for several sets of initial and boundary conditions corresponding to succeedingly more complex physical phenomena in closed and open domains. The problems we will consider include linear and nonlinear box modes, forced nonlinear box modes, and linear and nonlinear Rossby waves. The sequence of linear problems (box modes and Rossby waves) serve as pivotal calculations for which no boundary values of vorticity are formally required. With the addition of nonlinearity, both accuracy and stability of model calculations can be assessed as functions of ϵ for closed-domain problems in which strict conservation laws apply (nonlinear and forced nonlinear box modes), and totally open domain problems in which interaction with the surrounding environment is possible and the question of computational boundary conditions arises (nonlinear Rossby waves). The former experiments are the most easily understood. The latter series of tests—particularly the nonlinear Rossby waves with mean advection—are those most relevant to future open ocean modeling applications.

TABLE I

Maximum RMS Error Measures—RMS(ψ'), RMS(ζ'), and NDIF (NRG)—for the Finite-Difference (FD), Finite-Element (FE), and Pseudospectral (PS) Models as a Function of Problem Class, Duration of Experiment, and the Associated Nondimensional Parameters[a]

Expt	ϵ	Δ	x_B	N	ν	η	m	n		Duration	RMS(ψ')	RMS(ζ')	NDIF(NRG)	Comments
									Linear and nonlinear box modes					
1	0	$2^{1/2}$	$2^{1/2}\pi$	33	$16(2)^{1/2}$	64	1	1	FD	5	10.8×10^{-2}	9.4×10^{-2}	8.1×10^{-4}	
									FE	5	6.0×10^{-2}	5.2×10^{-2}	2.1×10^{-4}	
				17	$8(2)^{1/2}$				PS	5	6.2×10^{-2}	5.4×10^{-2}	1.9×10^{-4}	
2	0	$2^{1/2}$	$2^{1/2}\pi$	33	$16(2)^{1/2}$	32	1	1	FD	5	7.8×10^{-2}	6.8×10^{-2}	6.6×10^{-4}	
									FE	5	25×10^{-2}	21×10^{-2}	16×10^{-4}	
				17	$8(2)^{1/2}$				PS	5	25×10^{-2}	22×10^{-2}	16×10^{-4}	
3	0	$2^{1/2}$	$2^{1/2}\pi$	33	$16(2)^{1/2}$	128	1	1	FD	5	15×10^{-2}	27×10^{-2}	72×10^{-5}	
									FE	5	1.3×10^{-2}	2.3×10^{-2}	4.2×10^{-5}	
				17	$8(2)^{1/2}$				PS	5	1.5×10^{-2}	1.4×10^{-2}	2.4×10^{-5}	
4	0	$2(2)^{1/2}$	$2(2)^{1/2}\pi$	33	$8(2)^{1/2}$	64	2	2	FD	5	51×10^{-2}	46×10^{-2}	24×10^{-4}	
									FE	5	4.2×10^{-2}	5.5×10^{-2}	7.7×10^{-4}	
				17	$4(2)^{1/2}$				PS	5	5.3×10^{-2}	5.1×10^{-2}	4.0×10^{-4}	
5	0	$3(2)^{1/2}$	$3(2)^{1/2}\pi$	33	$16(2)^{1/2}/3$	64	3	3	FD	5	96×10^{-2}	93×10^{-2}	5.2×10^{-3}	
									FE	5	2.5×10^{-2}	7.6×10^{-2}	3.0×10^{-3}	
				17	$8(2)^{1/2}/3$				PS	5	3.3×10^{-2}	5.8×10^{-2}	3.7×10^{-3}	
6	0.2	$2^{1/2}$	$2^{1/2}\pi$	33	$16(2)^{1/2}$	64	1	1	FD	5	18×10^{-2}	16×10^{-2}	11×10^{-3}	Sundstrom
									FD	5	18×10^{-2}	16×10^{-2}	9.3×10^{-3}	$\zeta_\Sigma = \zeta_B$
									FD	5	18×10^{-2}	16×10^{-2}	11×10^{-3}	Kreiss
									FE	5	8.4×10^{-2}	10×10^{-2}	3.0×10^{-3}	
				17	$8(2)^{1/2}$				PS	5	35×10^{-2}	34×10^{-2}	2.4×10^{-3}	
7	0.4	$2^{1/2}$	$2^{1/2}\pi$	33	$16(2)^{1/2}$	64	1	1	FD	5	8.6×10^{-1}	8.3×10^{-1}	1.6×10^{-2}	
									FE	5	12×10^{-1}	18×10^{-1}	2.6×10^{-2}	unstable
									FE	5	12×10^{-1}	11×10^{-1}	2.6×10^{-3}	filter
									PS	[2.5]				
									PS	5	12×10^{-1}	11×10^{-1}	1.2×10^{-2}	filter

8	0.2	$2(2)^{1/2}$	$2(2)^{1/2}\pi$	33	$8(2)^{1/2}$	64	2	2		FD	5	29×10^{-2}	28×10^{-2}	35×10^{-2}	
										FE	5	6.5×10^{-2}	12×10^{-2}	2.3×10^{-3}	
										PS	5	30×10^{-2}	35×10^{-2}	-1.0×10^{-3}	
9	0.2	$2^{1/2}$	$2^{1/2}\pi$	33	$16(2)^{1/2}$	128	1	1		FD	5	1.4×10^{-1}	1.2×10^{-1}	10×10^{-3}	
										FE	5	2.8×10^{-1}	2.5×10^{-1}	4.5×10^{-3}	
				17	$8(2)^{1/2}$					PS	5	3.1×10^{-1}	3.0×10^{-1}	2.4×10^{-3}	

Forced nonlinear box modes

	ϵ	A	x_B	N	ν	η	a	b	c		Duration	RMS(ψ')	RMS(ζ')	NDIF(NRG)	Comments
10	0.2	1.0	π	17	16	64	$1/2^{1/2}$	$1/2^{1/2}$	1/2	FD	2	1.9×10^{-2}	5.2×10^{-2}	2.8×10^{-2}	
										FE	2	1.1×10^{-2}	6.5×10^{-2}	1.2×10^{-2}	
										PS	2	1.0×10^{-3}	1.6×10^{-2}	1.4×10^{-2}	
11	0.2	1.0	π	33	32	64	$1/2^{1/2}$	$1/2^{1/2}$	1/2	FD	2	4.4×10^{-3}	1.4×10^{-2}	6.3×10^{-3}	
										FE	2	9.0×10^{-3}	2.0×10^{-2}	14×10^{-3}	
										PS	2	10×10^{-3}	1.5×10^{-2}	14×10^{-3}	
12	0.2	1.0	π	33	32	128	$1/2^{1/2}$	$1/2^{1/2}$	1/2	FD	2	9.6×10^{-3}	2.0×10^{-2}	-9.5×10^{-3}	
										FE	2	2.6×10^{-3}	1.9×10^{-2}	2.9×10^{-3}	
										PS	2	2.3×10^{-3}	0.4×10^{-2}	3.5×10^{-3}	

Linear and nonlinear Rossby waves

Expt	ϵ	A	x_B	N	ν	η	k	l	γ		Duration	RMS(ψ')	RMS(ζ')	NDIF(NRG)	Comments
13	0.0	3.5	3.5π	33	32/3.5	128	$3/13^{1/2}$	$2/13^{1/2}$	0	FD	5	160×10^{-3}	145×10^{-3}	-150×10^{-3}	
										FE	5	6.3×10^{-3}	12×10^{-3}	6.0×10^{-3}	
				17	16/3.5					PS	5	8.3×10^{-3}	8.2×10^{-3}	8.0×10^{-3}	
14	0.4	3.5	3.5π	17	16/3.5	64	$3/13^{1/2}$	$2/13^{1/2}$	0	FD	5	58×10^{-2}	52×10^{-2}	-45×10^{-2}	
										FE	5	6.2×10^{-2}	6.8×10^{-2}	6.2×10^{-2}	
										PS	[4.5]				
										PS	5	1.9×10^{-2}	1.9×10^{-2}	2.1×10^{-2}	filter

TABLE I—*Continued*

Expt	ϵ	Δ	x_B	N	ν	η	k	l	γ		Duration	RMS(ψ')	RMS(ζ')	NDIF(NRG)	Comments
15	0.4	3.5	3.5π	33	32/35	64	$3/13^{1/2}$	$2/13^{1/2}$	0	FD	5	14×10^{-2}	13×10^{-2}	-14×10^{-2}	
										FE	5	8.3×10^{-2}	9.2×10^{-2}	9.0×10^{-2}	
										PS	[3.0]				
										PS	5	2.0×10^{-2}	2.1×10^{-2}	2.1×10^{-2}	filter
16	0.4	3.5	3.5π	33	32/3.5	128	$3/13^{1/2}$	$2/13^{1/2}$	0	FD	5	16×10^{-2}	15×10^{-2}	-16×10^{-2}	
										FD	5	15×10^{-2}	15×10^{-2}	-15×10^{-2}	filter
										FE	5	2.6×10^{-2}	4.2×10^{-2}	1.8×10^{-2}	
										FE	5	1.7×10^{-2}	2.0×10^{-2}	1.9×10^{-2}	filter
				17	16/3.5					PS	[4.5]				
				17	16/3.5					PS	5	0.5×10^{-2}	0.5×10^{-2}	0.5×10^{-2}	filter
17	0.4	3.5	3.5π	33	32/3.5	128	$3/13^{1/2}$	$2/13^{1/2}$	0.5	FD	5	27×10^{-3}	20×10^{-2}	-38×10^{-3}	
										FD	5	33×10^{-3}	44×10^{-2}	12×10^{-3}	filter
										FE	5	7.0×10^{-3}	9.4×10^{-2}	5.2×10^{-3}	
										FE	5	5.6×10^{-3}	6.0×10^{-2}	6.2×10^{-3}	filter
				17	16/3.5					PS	[4.0]				
				17	16/3.5					PS	5	4.1×10^{-3}	2.9×10^{-2}	9.6×10^{-3}	filter
18	0.4	3.5	3.5π	33	32/3.5	128	$3/13^{1/2}$	$2/13^{1/2}$	-0.5	FD	5	410×10^{-4}	190×10^{-3}	-100×10^{-3}	
										FE	5	46×10^{-4}	34×10^{-3}	13×10^{-3}	
				17	16/3.5					PS	[4.0]				
				17	16/3.5					PS	5	9.0×10^{-4}	6.0×10^{-3}	-1.0×10^{-3}	filter
19	0.8	3.5	3.5π	33	32/3.5	128	$3/13^{1/2}$	$2/13^{1/2}$	0	FD	5	160×10^{-3}	17×10^{-2}	-160×10^{-3}	
										FD	5	150×10^{-3}	16×10^{-2}	-140×10^{-3}	filter
										FE	5	42×10^{-3}	5.4×10^{-2}	27×10^{-3}	
										FE	5	33×10^{-3}	3.5×10^{-2}	25×10^{-3}	filter
				17	16/3.5					PS	[2.0]				
				17	16/3.5					PS	5	6.7×10^{-3}	1.1×10^{-2}	7.4×10^{-3}	filter

20	0.4	3.5	3.5π	33	32/3.5	128	$1/2^{1/2}$	$1/2^{1/2}$	0	FD	5	59×10^{-3}	79×10^{-3}	45×10^{-3}	
										FE	5	23×10^{-3}	39×10^{-3}	-4.0×10^{-3}	
				17	16/3.5					PS	5	3.8×10^{-3}	6.8×10^{-3}	-3.0×10^{-3}	filter
21	0.4	3.5	3.5π	33	33/3.5	128	$1/2^{1/2}$	$1/2^{1/2}$	0.5	FD	5	5.2×10^{-3}	9.4×10^{-2}	12×10^{-3}	
										FE	5	5.5×10^{-3}	9.4×10^{-2}	7.2×10^{-3}	
				17	16/3.5					PS	5	3.0×10^{-3}	1.8×10^{-2}	4.7×10^{-3}	filter
22	0.4	3.5	3.5π	33	32/3.5	128	$-3/13^{1/2}$	$+2/13^{1/2}$	0	FD	5	160×10^{-3}	160×10^{-3}	-160×10^{-3}	
										FE	5	26×10^{-3}	43×10^{-3}	18×10^{-3}	
				17	16/3.5					PS	5	4.7×10^{-3}	5.3×10^{-3}	4.8×10^{-3}	filter
23	0.4	3.5	3.5π	33	32/3.5	128	$-3/13^{1/2}$	$2/13^{1/2}$	0.5	FD	5	27×10^{-3}	19×10^{-3}	-39×10^{-3}	
										FE	5	7.2×10^{-3}	9.7×10^{-2}	5×10^{-3}	
				17	16/3.5					PS	5	3.8×10^{-3}	2.8×10^{-2}	9.3×10^{-3}	filter
24	0.4	3.5	3.5π	33	32/3.5	128	$3/13^{1/2}$	$2/13^{1/2}$	-1.5	FD	5	110×10^{-1}	240×10^{-3}	-110×10^{-1}	
										FE	5	24×10^{-4}	40×10^{-3}	38×10^{-4}	
				17	16/3.5					PS	5	6.3×10^{-4}	9.6×10^{-3}	-6.2×10^{-4}	filter
25	0.4	7.0	7.0π	33	32/3.5	128	$3/13^{1/2}$	$2/13^{1/2}$	0	FD	5	740×10^{-3}	580×10^{-3}	-100×10^{-3}	
										FE	5	18×10^{-3}	30×10^{-3}	-2.2×10^{-3}	
										PS	5	5.8×10^{-3}	7.4×10^{-3}	3.1×10^{-3}	filter
26	0.4	7.0	7.0π	33	32/3.5	128	$3/13^{1/2}$	$2/13^{1/2}$	0.5	FD	5	62×10^{-3}	47×10^{-2}	-170×10^{-3}	
										FE	5	7.0×10^{-3}	25×10^{-2}	18×10^{-3}	
										PS	5	1.9×10^{-3}	2.6×10^{-2}	6.3×10^{-3}	filter
27	0.4	3.5	3.5π	17	16/3.5	128	$3/13^{1/2}$	$2/13^{1/2}$	0	FD	5	600×10^{-3}	540×10^{-3}	-460×10^{-3}	
										FE	5	18×10^{-3}	37×10^{-3}	-6.6×10^{-3}	
										PS	5	4.8×10^{-3}	5.3×10^{-3}	5.0×10^{-3}	filter
28	0.4	3.5	3.5π	17	16/3.5	128	$3/13^{1/2}$	$2/13^{1/2}$	0.5	FD	5	120×10^{-3}	53×10^{-2}	-120×10^{-3}	
										FE	5	30×10^{-3}	45×10^{-2}	-36×10^{-3}	
										PS	5	4.1×10^{-3}	2.9×10^{-2}	9.8×10^{-3}	filter

[a] The first seven columns refer to the experiment number and the quantities ϵ, A, x_B, N, ν, and η which are, respectively, the Rossby number, the number of half wavelengths of the reference solution within the domain, the nondimensional basin size, the number of spatial degrees of freedom in each direction and nondimensional measures of the spatial and temporal resolution. Intermediate columns are reserved for problem-dependent parameters which have been introduced in Sections 4–6.

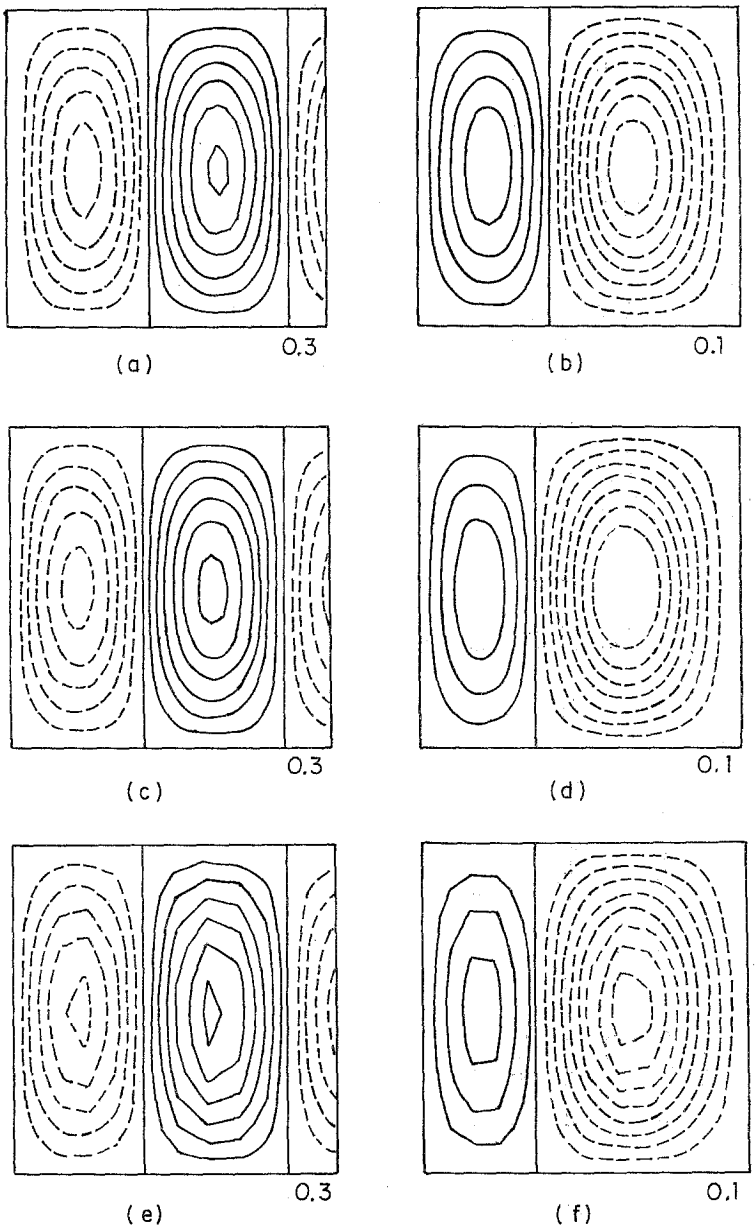

FIG. 1. Linear box mode solution at $t = 10$ periods with $(\eta, m, n) = (128,1,1)$. (a, b), (ζ, ψ) FD model, $\nu = 16(2)^{1/2}$, CI = 0.3, 0.1); (c, d), (ζ, ψ): FE model, $\nu = 16(2)^{1/2}$, CI = (0.3, 0.1); (e, f) (ζ, ψ): PS model, $\nu = 8(2)^{1/2}$, CI = (0.3, 0.1).

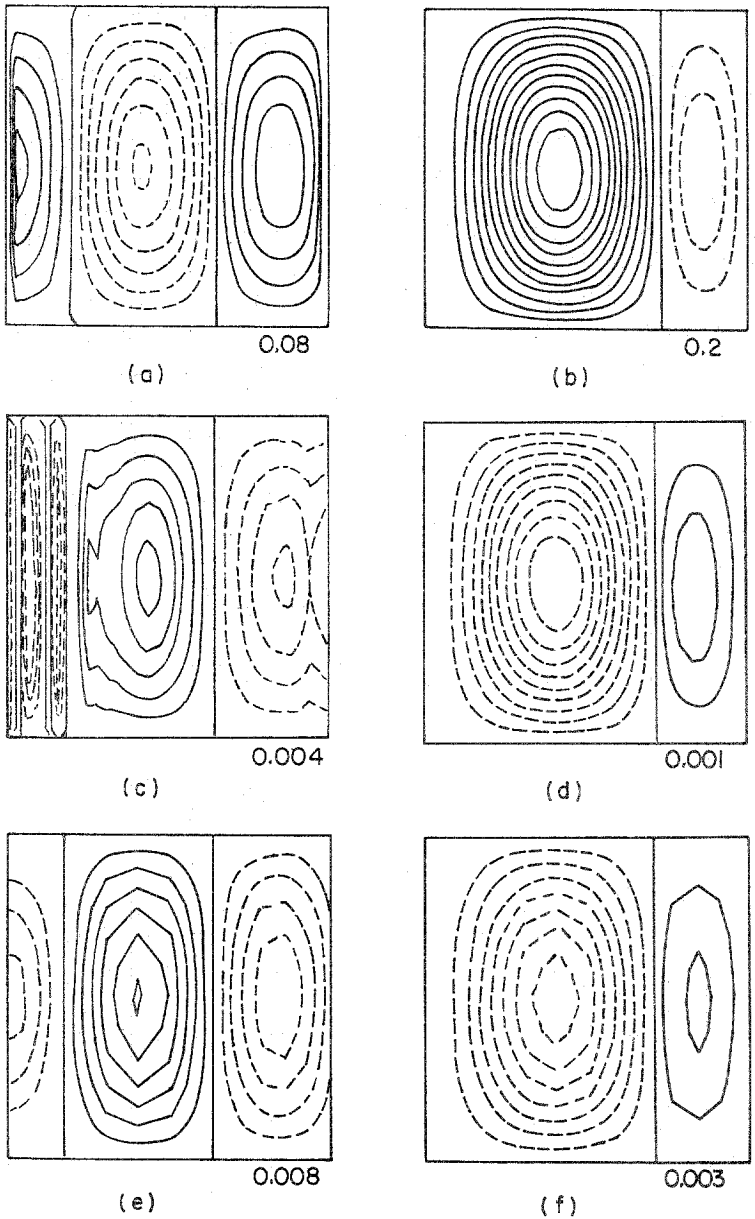

FIG. 2. As Fig. 1. (a, b), (ζ', ψ'): FD model, $\nu = 16(2)^{1/2}$, CI = (0.08, 0.02); (c, d), (ζ', ψ'): FE model, $\nu = 16(2)^{1/2}$, CI = (4.0, 1.0) $\times 10^{-3}$; (e. f), (ζ', ψ'): PS model, $\nu = 8(2)^{1/2}$, CI = (8.0, 3.0) $\times 10^{-3}$.

Each problem thus defined has been solved using three independent (and quite different) numerical techniques. The finite-difference (FD) scheme is second-order accurate in space and time and has the advantage of being easily coded. It should, in addition, be the most efficient of the three models for a fixed number of spatial degrees of freedom. The finite-element (FE) method, though somewhat more complicated than the FD scheme, is known to be of fourth order for certain advective problems [25]. In general, we expect smaller errors with the FE model, but at a slightly higher computational cost. Lastly, pseudospectral (PS) approximation techniques [22] offer greatly reduced spatial truncation errors in comparison to both of the other two methods. The PS model is, therefore, formally the most accurate but thereby it may be subject to instabilities not seen in the FD formulation—see, for instance, Section 6. Of the three models, it is also the most difficult to code (although it can be made comparably efficient if care is taken to optimize the spectral transforms).

Since analytic or perturbation solutions are available for many of the prototype physical problems examined herein, direct measures of numerical error are available for each model. Of particular interest are the RMS errors in streamfunction and vorticity, and the normalized difference in integrated kinetic energy as a function of time; these area-integrated error measures are defined as

$$\mathrm{RMS}(\psi') = \left\{ \iint (\psi_c - \psi_a)^2 \, dA \Big/ \iint (\psi_a)^2 \, dA \right\}^{1/2}, \tag{4a}$$

$$\mathrm{RMS}(\zeta') = \left\{ \iint (\zeta_c - \zeta_a)^2 \, dA \Big/ \iint (\zeta_a)^2 \, dA \right\}^{1/2}, \tag{4b}$$

and

$$\mathrm{NDIF(NRG)} = \left\{ \iint | \nabla\psi_c |^2 \, dA - \iint | \nabla\psi_a |^2 \, dA \right\} \Big/ \iint | \nabla\psi_a |^2 \, dA, \tag{4c}$$

where subscripts c and a refer to the computed and analytic solutions, respectively, and a primed quantity represents a difference from the reference solution. Using error measures of this sort, it is possible to ascertain the accuracy of each model.

Table I summarizes the results of all the experiments as a function of problem type and the associated nondimensional parameters. The first nine columns of Table I refer to the experiment number and the (not necessarily independent) quantities

(i)	ϵ	Rossby number
(ii)	$x_B = y_B$	Nondimensional basin size
(iii)	N	Number of spatial degrees of freedom in each direction
(iv)	$h = x_B/(N-1)$	Nondimensional mesh interval
(v)	Δ	Number of half wavelengths or turning points of the reference solution within the domain (nondimensional measure of the structure of the reference solution)

(vi)	$\nu = (N-1)/\Delta$	Nondimensional spatial resolution (number of degrees of freedom per turning point of the reference solution)
(vii)	Δt	Nondimensional time increment
(viii)	η	Nondimensional temporal resolution (number of time steps per period of the reference solution).

The last four columns tabulate the duration of the experiment (in periods) and the final values of the three error measures defined above. The duration of simulations which suffered numerical instability are denoted by brackets. No RMS error values are listed for these experiments. Intermediate columns of Table I are reserved for special parameters representative of each problem class. These will be introduced in Sections 4 through 6.

Accompanying Table I is a series of figures which show in more detail the results of one experiment for each problem category. Figures 1 through 3 are typical. The first two figures give contour plots of ζ and ψ, and ζ' and ψ', respectively, at the end of the simulations for each model. Figure 3 shows the corresponding variation with time of RMS(ζ') and RMS(ψ') for each model. Contouring intervals are given in the figure captions and at the lower right-hand corner of each contour map.

The former (contour) plots give a visual estimate of the wavenumber content of

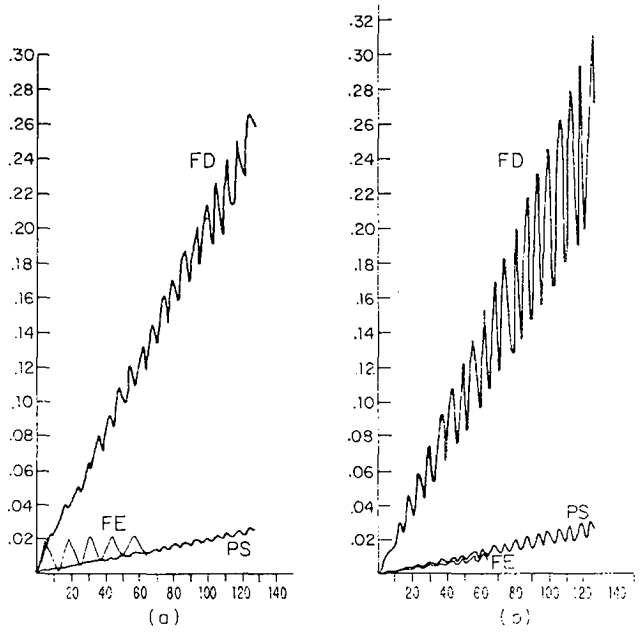

FIG. 3. As Fig. 1. (a, b), RMS(ζ', ψ'): FD model, $\nu = 16(2)^{1/2}$, $0 \leqslant t \leqslant 10$ periods; FE model, $\nu = 16(2)^{1/2}$, $0 \leqslant t \leqslant 5$ periods; PS model, $\nu = 8(2)^{1/2}$, $0 \leqslant t \leqslant 10$ periods.

the computed solution (and hence an estimate of its formal spatial accuracy) and reveal any localized features (physical or numerical) that might occur. This is particularly important in those nonlinear experiments for which only approximate or linearized reference solutions are available and for which the RMS errors are therefore difficult to interpret.

3. Model Formulation

3.1. *Finite-Difference Model*

A traditional discrete formulation of Eq. (3) results by approximating all derivatives by second-order centered finite differences. The advantages of finite differences are the simplicity of the required coding and our accumulated experience of using this classical technique. With centered (leapfrog) time differencing, the vorticity and Poisson equations become

$$\zeta^{k+1} = \zeta^{k-1} - \frac{2\Delta t\epsilon}{h^2} J^*(\psi^k, \zeta^k) - \frac{\Delta t}{h} \delta_x \psi^k, \tag{5a}$$

and

$$\delta_{xx}\psi^{k+1} + \delta_{yy}\psi^{k+1} = h^2\zeta^{k+1}, \tag{5b}$$

where finite-difference operators $\delta_x(\psi^k) = \psi^k_{i+1,j} - \psi^k_{i-1,j}$ and $\delta_{xx}(\psi^x) = \psi^k_{i+1,j} - 2\psi^k_{i,j} + \psi^k_{i-1,j}$. The Arakawa [26] Jacobian J^* is given by the finite-difference approximation to the equivalent form $\frac{1}{3}\{[\psi_x\zeta_y - \psi_y\zeta_x] + [(\psi\zeta_y)_x - (\psi\zeta_x)_y] + [-(\psi_y\zeta)_x + (\psi_x\zeta)_y]\}$. This expression conserves vorticity, energy, and enstrophy when integrated over a closed domain The Poisson equation (5b) with Dirichlet boundary conditions is approximated by the standard five-point Laplacian operator and solved with the NCAR cyclic reduction subroutine package Finite differences are of second-order accuracy, so the total discretization error is $O(h^2 + \Delta t^2)$.

For linear problems ($\epsilon = 0$), vorticity on the boundary Σ does not enter the problem in either the vorticity equation or the Poisson equation. For nonlinear problems ($\epsilon \neq 0$), vorticity is specified at inflow points according to the Charney–Fjortoft–von Neumann boundary condition [19]. Centered finite differences require boundary data everywhere, and in contrast to the analytic problem, some auxiliary relationship (that is, a computational boundary condition) must be assumed *at outflow points* in order to determine the vorticity there (unless an iterative technique is used to fix ζ on outflow).

Optimally, the computational boundaries of an open ocean model should be transparent to signals impinging on them. Thus, the formation of boundary layers on, or wave reflections from, the boundary are undesirable. The most successful computational boundary condition considered in this study is

$$\zeta_B^k + \zeta^k_{B-2} = \zeta^{k+1}_{B-1} + \zeta^{k-1}_{B-1} \tag{6}$$

which was introduced by Sundstrom [17]. Here B, $B-1$, and $B-2$ represent a boundary point and its first and second normal interior neighbors. Davies [18] demonstrated the stability properties of this closure for a variety of nonlinear problems.

There are several possible physical interpretations of statement (6): Either (a) it is equivalent to equating the time and spatial averages of ζ at point $B-1$ (a kind of smoothness condition at outflow); (b) it is equivalent to $\zeta_{tt} = c^2\zeta_{xx}$, where $c = \Delta x/\Delta t$ (a "local" wave equation); or (c) it is a low-order spatial extrapolation scheme.

In order to implement the Sundstrom/Davies formula, the quantity ζ_{B-1}^{k+1} is eliminated by application of the vorticity equation evaluated at the point $B-1$, $t = k\,\Delta t$. This yields an implicit set of equations for the boundary vorticity. Formally, this requires the inversion of a heptadiagonal matrix with cyclic ordering of the points. However, it can be shown that by elimination of those boundary points which are corner neighbors, a simple tridiagonal system results, provided there is at least one inflow point (Appendix). Note that the boundary vorticity is calculated after the interior vorticity and the streamfunction.

Other computational boundary conditions investigated in this study are the extrapolation $\zeta_B{}^k = 2\zeta_{B-1}^{k-1} - \zeta_{B-2}^{k-1}$ [13] and the condiion $\zeta_B = \zeta_a$ corresponding to the exact specification of the outflow vorticity. Note once again that these computational boundary conditions are used to determine values of vorticity at outflow boundary points only; elsewhere on the boundary, independent values of vorticity are supplied in accordance with the Charney–Fjortoft–von Neumann prescription.

3.2. *Finite-Element Model*

In the finite-element formulation, we assume a set of basic functions consisting of piecewise polynomials, the simplest being piecewise linear elements arranged in a rectangular lattice. In one dimension, each element is a chapeau or hill function, and in two dimensions, a pyramidal function, each centered on the lattice point with base width $2h$ [25]. Then the basis functions have the property

$$\begin{aligned} \phi_q(\mathbf{z}_p) &= 1 \quad \text{if} \quad p = q, \\ &= 0 \quad \text{if} \quad p \neq q, \end{aligned} \tag{7}$$

where $\mathbf{z}_p$ is the pth lattice point. All fields can be expressed in terms of a summation of the basis functions; for instance,

$$\psi(\mathbf{x}, t) = \sum_q \psi_q(t)\,\phi_q(\mathbf{x}), \tag{8}$$

$$\zeta(\mathbf{x}, t) = \sum_q \zeta_q(t)\,\phi_q(\mathbf{x}), \tag{9}$$

where $\mathbf{x}$ is a general point within the domain.

The weights ψ_q and ζ_q are obtained by the Galerkin procedure. Substitute (8) and (9) into the vorticity equation, multiply by a basis function, and integrate over the entire region. Since each element overlaps those adjacent to it, in general, each equation will contain terms from its eight neighbors.

For closed-domain problems, we use centered time differences. The resulting finite-element form of the vorticity equation is

$$M(\zeta^{k+1}) = M(\zeta^{k-1}) - 2\Delta t\, Q^k = P^{k+1}, \tag{10a}$$

where

$$Q^k = \frac{\epsilon}{h^2} J^*(\psi^k, \zeta^k) - \frac{1}{2h} W^{(y)}\delta_x(\psi^k).$$

In partially and completely open domains, however, a second-order Adams–Bashforth time-differencing scheme is used to avoid computational instability. In such cases,

$$M(\zeta^{k+1}) = M(\zeta^x) - \Delta t\{\tfrac{3}{2}Q^x - \tfrac{1}{2}Q^{x-1}\}. \tag{10b}$$

The mass matrix M has the entries $M_{pq} = \iint \phi_p\phi_q\, dA$. M is factorable into two parts, $M = W^{(x)} \otimes W^{(y)}$, where $\otimes$ denotes tensor multiplication and the matrices $W^{(x)}$ and $W^{(y)}$ are tridiagonal with the local form $\frac{1}{6}(1\ 4\ 1)$. The operator $W^{(x)} \otimes W^{(y)}$ can be interpreted to mean successive multiplications—first rowwise, then columnwise—by the matrix $W = W^{(x)} = W^{(y)}$. Note that the superscripts (x) and (y) refer to the order in which the tridiagonal multiplications are done. At each time step, therefore, Eq. (10) can be written

$$M(\zeta^{k+1}) = W^{(x)} \otimes W^{(y)}(\zeta^{k+1}) = P^{k+1},$$

where ζ^{k+1} is the $N \times N$ matrix of values of ζ at time step $(k+1)$. In this form, it is clear that Eq. (10a) is equivalent to two tridiagonal matrix systems each of size $N \times N$. The mass matrix can therefore be readily inverted. Note that if W is set equal to the identity matrix, Eq. (10a) reduces to the finite-difference form (5a). The Jacobian term is precisely the Arakawa Jacobian employed with finite differences [26]. In fact, the Arakawa form is derivable from the finite-element formulation [27].

Fix [25] has shown that linear elements for the linearized advective equation $\zeta_t + U\zeta_x = 0$ produce fourth-order accurate phase errors. To maintain this accuracy for the vorticity equation, the solution of the Poisson equation for the streamfunction must also be of fourth order. This is accomplished by the method of deferred corrections [28]. Note that

$$K(\psi) = h^2\,\nabla^2\psi + \frac{1}{12}h^4\left(\nabla^4 - 2\frac{\partial^4}{\partial x^2\,\partial y^2}\right)\psi + O(h^6),$$

where K is the usual five-point Laplacian

$$K = \begin{pmatrix} 0 & 1 & 0 \\ 1 & -4 & 1 \\ 0 & 1 & 0 \end{pmatrix}.$$

Therefore two successive Poisson solutions yield ψ to fourth order in the following manner. First, obtain a second-order solution, ψ_1, from $K(\psi_1) = h^2\zeta$. Then, a fourth-order estimate of ψ is the solution to

$$K(\psi) = h^2\zeta + \frac{h^4}{12}\left(\nabla^2\zeta - 2\frac{\partial^4}{\partial x^2 \partial y^2}\psi_1\right). \tag{11}$$

Finite elements require more computational work per time step than do finite differences. First, two tridiagonal inversions must be performed to determine the vorticity field, contrasted with a simple direct substitution in finite differences. Second, two calls must be made to the Poisson solver instead of one. The significant increase in accuracy plus the virtue of using a technique based on a variational principle justify this increased computational effort in many applications, as indeed they will here (see, for instance, Section 6).

In the finite-element model, vorticity boundary conditions are implemented in the following manner. For ease of presentation, we introduce three types of points and their respective computational molecules m, that is, their local contribution to mass matrix M:

(a) interior points
$$m_{\mathrm{I}} = 1/36 \begin{pmatrix} 1 & 4 & 1 \\ 4 & \underline{16} & 4 \\ 1 & 4 & 1 \end{pmatrix} \tag{12a}$$

(b) regular boundary points
$$m_{\mathrm{E}} = 1/36 \begin{pmatrix} 0 & 1 & 2 \\ 0 & 4 & \underline{8} \\ 0 & 1 & 2 \end{pmatrix} \text{ (Eastern wall)} \tag{12b}$$

(c) corner points
$$m_{\mathrm{SE}} = 1/36 \begin{pmatrix} 0 & 0 & 0 \\ 0 & 1 & 2 \\ 0 & 2 & \underline{4} \end{pmatrix} \text{ (Southeast corner)} \tag{12c}$$

The lattice point associated with the given element is denoted by boldface type. Analogous computational molecules exist for regular boundary points on the northern, southern, and western walls and for the southwest, northwest, and northeast corner points.

Assume first that vorticity is specified everywhere on the boundary (corresponding to inflow everywhere) and that solutions are needed only for the interior points. It is then easy to show that this is equivalent to the system of equations:

$$M_4(\zeta^{n+1}) = P_4, \tag{13}$$

where

$$
\begin{aligned}
P_4 &= P && \text{for interior points,} \\
&= P - \begin{pmatrix} 1 \\ 4 \\ 1 \end{pmatrix} \zeta_B/36 && \text{at (eastern) boundary,} \\
&= P - \begin{pmatrix} 0 & 0 & 1 \\ 0 & 0 & 4 \\ 1 & 4 & 1 \end{pmatrix} \zeta_B/36 && \text{at (southeast) corner.}
\end{aligned} \tag{14}
$$

ζ_B is the specified boundary vorticity, and $M_4 = W_4^{(x)} \otimes W_4^{(y)}$, where W_4 $(= W_4^{(x)} = W_4^{(y)})$ is the $(N-2) \times (N-2)$ tridiagonal matrix

$$
W_4 = \frac{1}{6} \begin{pmatrix} 4 & 1 & & & \\ 1 & 4 & 1 & & \\ & 1 & 4 & 1 & \\ & & 1 & 4 & 1 \\ & & & 1 & 4 \end{pmatrix}. \tag{15}
$$

The subscript (4) refers to the corner terms in (15).

Next consider the case where vorticity is *not* specified anywhere on the boundary, as in a basin totally enclosed by solid and/or outflow sides. Here solutions are sought for the entire field (interior, boundary, and corner points). It is then easy to show that the combined system including contributions of the form (12a)–(12c) is equivalent to

$$
M_2(\zeta^{k+1}) = P_2, \tag{16}
$$

where $M_2 = W_2^{(x)} \otimes W_2^{(y)}$, and

$$
W_2 = \frac{1}{6} \begin{pmatrix} 2 & 1 & & & \\ 1 & 4 & 1 & & \\ & 1 & 4 & 1 & \\ & & 1 & 4 & 1 \\ & & & 1 & 2 \end{pmatrix} \tag{17}
$$

is now $N \times N$.

These two cases represent extreme situations—either all inflow, or all outflow (and/or solid boundaries). We seek a method which will allow a general mix of

inflow and outflow sections around the boundary. We can do this by defining a new matrix, $M_{7/2}$, which has the computational structure

$$\begin{aligned} M_{7/2} &= m_{\mathrm{I}} && \text{for points } \textit{not} \text{ at or adjacent to the boundary } (i, j \neq 1, 2, N-1, N), \\ &= m_{\mathrm{I}} - \tfrac{1}{2}m_{\mathrm{E}} && \text{for interior points adjacent to the (eastern) boundary but not near a corner } (i = N-1, j \neq 2, \text{ or } N-1), \\ &= m_{\mathrm{I}} - \tfrac{1}{2}m_{\mathrm{E}} - \tfrac{1}{2}m_{\mathrm{S}} + \tfrac{1}{4}m_{\mathrm{SE}} && \text{for interior corner (southeast) points } (i = N-1, j = 2), \end{aligned} \tag{18}$$

and so on for points adjacent to other boundaries and corners. It can be shown that this new formulation decouples the determination of the interior vorticity from that of the boundary vorticity and is equivalent to

$$M_{7/2}(\zeta^{k+1}) = P_{7/2}\,, \tag{19}$$

where $P_{7/2}$ has the same relationship to P as $M_{7/2}$ to M given in (18). In addition, $M_{7/2} = W_{7/2}^{(x)} \otimes W_{7/2}^{(y)}$, where

$$W_{7/2} = \frac{1}{6}\begin{pmatrix} 7/2 & 1 & & & \\ 1 & 4 & 1 & & \\ & 1 & 4 & 1 & \\ & & 1 & 4 & 1 \\ & & & 1 & 7/2 \end{pmatrix}.$$

and all of the unknowns are interior points. In short, we use the known dynamic [illegible] from the other.

Furthermore, given the interior values of vorticity from the inversion of $M_{7/2}$, each of the four boundaries can be decoupled from its neighbors by using the identical strategy. That is, using cornerpoint dynamic relations—with computational structure as suggested by (12c)—the cornerpoint values of vorticity can be eliminated from the solution of the remaining boundary points. The resulting matrix equation—for instance, for the eastern boundary minus its cornerpoints—can be written

$$\begin{pmatrix} 7 & 2 & & & & \\ 2 & 8 & 2 & & & \\ & 2 & 8 & 2 & & \\ & & 2 & 8 & 2 & \\ & & & 2 & 8 & 2 \\ & & & & 2 & 7 \end{pmatrix} \zeta_{\mathrm{E}} = R_{\mathrm{E}}\,. \tag{20}$$

where ζ_E is the (column) matrix of unknown vorticity values along the eastern boundary (minus corners) and vector R_E contains only known information from previous time steps—i.e., the right-hand side of (10b) evaluated at the eastern boundary points (including corners)—and terms reflecting the newly updated values of interior vorticity. When, as prescribed by the C–F–VN criterion, values of vorticity are to be imposed at a particular boundary point, the appropriate row in matrix equation (20) and element in R_E—the ith, say—are replaced, respectively, by the ith row of the identity matrix and the desired value of vorticity. Each set of boundary values—minus cornerpoints—is obtained by an inversion of an analogous tridiagonal matrix equation. The cornerpoint values then follow algebraically.

In the finite-element approximation, the order of calculation is therefore the following: interior vorticity, vorticity at regular boundary points, vorticity at cornerpoints, and lastly the streamfunction. The reader should note, however, that this solution procedure does not strictly guarantee that values of vorticity on, or adjacent to, points of inflow be in exact dynamic balance.

3.3. *Pseudospectral Model*

We seek a (discrete) spectral solution to Eq. (3) subject to some appropriate set of boundary and initial conditions. For definiteness, consider specifying boundary values of streamfunction and vorticity in the manner first suggested by Charney, Fjortoft, and von Neumann [19]. That is, we take as given quantities the values of ψ everywhere along Σ, and ζ at those points along Σ characterized by mass influx. Boundary values of vorticity at outflow points are therefore unconstrained; they are computed as part of the calculation. Under these boundary conditions, a completely enclosed domain is a special case, one for which—owing to the absence of any inflow at all—vorticity need never be specified at any time along Σ. In analogy to the analytic problem, we make a computational distinction between problems contained within bounded regions and those characterized by partially or fully open domains.

3.3.1. *Closed Domain*

In a closed system, the advective terms in Eq. (3) are treated explicitly by a leapfrog time-differencing scheme. Under this second-order approximation, the vorticity and Poisson equations become, in the usual notation,

$$\begin{aligned} \zeta^{k+1} &= \zeta^{k-1} - 2\Delta t\{\epsilon J(\psi^k, \zeta^k) + \psi_x{}^k\} \\ &= R^{k+1}(x, y) \end{aligned} \tag{21}$$

and

$$\nabla^2\psi^{k+1} = \zeta^{k+1}. \tag{22}$$

In space, we adopt a pseudospectral approximation technique for which the dependent variables are expanded in a series of Chebyshev polynomials; that is, let

$$\psi^k(\hat{x}, \hat{y}) = \sum_{n=0}^{N} \sum_{m=0}^{N} a_{nm}^k T_n(\hat{x})\, T_m(\hat{y}), \qquad -1 \leqslant \hat{x}, \quad \hat{y} \leqslant +1, \tag{23a}$$

$$\zeta^k(\hat{x}, \hat{y}) = \sum_{n=0}^{N} \sum_{m=0}^{N} b_{nm}^k T_n(\hat{x})\ T_m(\hat{y}), \tag{23b}$$

and

$$R^k(\hat{x}, \hat{y}) = \sum_{n=0}^{N} \sum_{m=0}^{N} R_{nm}^k T_n(\hat{x})\ T_m(\hat{y}), \tag{23c}$$

where

$$\hat{x} = (2x - x_B)/x_B\,,$$
$$\hat{y} = (2y - y_B)/y_B\,,$$

and $T_n(\hat{x}) = \cos(n \cos^{-1} \hat{x})$ is the Chebyshev polynomial (of the first kind) of degree n, a function of the linearly stretched coordinates $\hat{x}$ and $\hat{y}$. On the collocation grid $(\hat{x}_p\,, \hat{y}_q) = (\cos(\pi p/N), \cos(\pi q/N))$, $0 \leqslant p, q \leqslant N$, this implies, for instance, that

$$\psi^k(\hat{x}_p\,, \hat{y}_q) = \sum_{n=0}^{N} \sum_{m=0}^{N} a_{nm}^k \cos\left\{\frac{\pi pn}{N}\right\} \cos\left\{\frac{\pi qm}{N}\right\},$$

demonstrating the important fact that a Chebyshev transform is equivalent to a cosine transform on the (nonuniform) collocation grid $(\hat{x}_p\,, \hat{y}_q)$ and as such can be implemented very efficiently using special forms of the fast Fourier transform algorithm [29].

Under these definitions, Eqs. (21) and (22) can be rewritten in terms of the spectral coefficients a_{nm}, b_{nm}, and R_{nm}:

$$b_{nm}^{k+1} = R_{nm}^{k+1}, \qquad 0 \leqslant n,\ \ m \leqslant N, \tag{24}$$

and

$$[a^{xx} + a^{yy}]_{nm}^{k+1} = b_{nm}^{k+1}, \qquad 0 \leqslant n,\ \ m \leqslant N, \tag{25}$$

where a_{nm}^{xx} and a_{nm}^{yy} satisfy

$$\frac{\partial^2}{\partial x^2}\,\psi = \frac{\partial^2}{\partial x^2} \sum_{n=0}^{N} \sum_{m=0}^{N} a_{nm} T_n(\hat{x})\ T_m(\hat{y})$$

$$= \sum_{n=0}^{N} \sum_{m=0}^{N} a_{nm}^{xx} T_n(\hat{x})\ T_m(\hat{y}),$$

and

$$\frac{\partial^2}{\partial y^2}\,\psi = \frac{\partial^2}{\partial y^2} \sum_{n=0}^{N} \sum_{m=0}^{N} a_{nm} T_n(\hat{x})\ T_m(\hat{y})$$

$$= \sum_{n=0}^{N} \sum_{m=0}^{N} a_{nm}^{yy} T_n(\hat{x})\ T_m(\hat{y}).$$

Unlike periodic models, the resulting spectral scheme can accomodate quite arbitrary boundary conditions on Σ. In the present bounded geometry, $\psi(x, y)$ is given on the boundary by some set of values, let us say ψ_Σ. In terms of the spectral coefficients a_{nm}, this is equivalent to requiring that

$$\sum_{n=0}^{N} \sum_{m=0}^{N} a_{nm} T_m(\hat{y}_q) = \psi_\Sigma(+1, y_q), \qquad 0 \leqslant q \leqslant N, \tag{26a}$$

$$\sum_{n=0}^{N} (-1)^n \sum_{m=0}^{N} a_{nm} T_m(\hat{y}_q) = \psi_\Sigma(-1, y_q), \qquad 0 \leqslant q \leqslant N, \tag{26b}$$

$$\sum_{m=0}^{N} \sum_{n=0}^{N} a_{nm} T_n(\hat{x}_p) = \psi_\Sigma(x_p, +1), \qquad 0 \leqslant p \leqslant N, \tag{26c}$$

and

$$\sum_{m=0}^{N} (-1)^m \sum_{n=0}^{N} a_{nm} T_n(\hat{x}_p) = \psi_\Sigma(x_p, -1), \qquad 0 \leqslant p \leqslant N, \tag{26d}$$

These conditions are imposed on the Poisson equation (22) by using the spectral analog of the tau method [30], that is, by neglecting the highest-order dynamic equations—those for $n = N - 1, N$ and $m = N - 1, N$—in (25). The remaining equations are then supplemented by boundary conditions (26a)–(26d), written in their equivalent Chebyshev series form, to close the problem. The resulting matrix equations are not sparse; however, they are quite easily diagonalized. The details of the solution have been given by Haidvogel and Zang [31] who show that, for sufficiently smooth fields and given accuracy, solutions to Poisson's equation can be computed at least as efficiently by these spectral techniques as by certain second- and fourth-order finite-difference methods.

Once the spectral coefficients a_{nm}^{k+1} have been determined, thus yielding $\psi(x, y)$ at the next time level, the velocity components $u = -\psi_y$ and $v = +\psi_x$ can be computed from well-known Chebyshev derivative relations. These in turn are combined to give the nonlinear term $J(\psi, \zeta) = \nabla \cdot (\mathbf{v}\zeta)$ by the simple pseudospectral procedure

$$\nabla \cdot (\mathbf{v}\zeta)|_{p,q} = \frac{\partial}{\partial x} [u(\hat{x}_p, \hat{y}_q)\ \zeta(\hat{x}_p, \hat{y}_q)] + \frac{\partial}{\partial y} [v(\hat{x}_p, \hat{y}_q)\ \zeta(\hat{x}_p\ \ \hat{y}_q)],$$

where the product $\mathbf{v}\zeta$ is determined locally by physical space multiplications on the collocation grid $(\hat{x}_p, \hat{y}_q)$ but the derivatives $\partial/\partial x$ and $\partial/\partial y$ are performed spectrally. The resulting scheme is of infinite-order accuracy and can be constructed so as to conserve any of the higher-order invariants such as energy and enstrophy; however, it retains the effects of high wavenumber aliasing at full strength [32]. The effects of aliasing can be identically removed, but at a large cost in computational efficiency (approximately a factor of 2).

3.3.2. *Open Domain*

In the spectral approximation, boundary conditions can only be correctly applied if the highest-order terms are treated in some way implicitly. For those problems in which the domain of integration is not bounded by an impermeable surface and for which, therefore, values of the vorticity are to be specified at points of inflow, this implies that the advective term must be treated somewhat differently than in a closed region. To do so, we adopt the following alternating direction implicit (ADI) time-differencing scheme.

$$\zeta^{k+1/2} + \frac{\epsilon\,\Delta t}{2}\frac{\partial}{\partial x}(u_0\zeta)^{k+1/2} = L_1(\zeta^{k-1/2})$$
$$= \zeta^k - \frac{\epsilon\,\Delta t}{2}\frac{\partial}{\partial y}(v_0\zeta)^k$$
$$- \frac{3}{4}\Delta t\{\epsilon\nabla\cdot[(\mathbf{v}-\mathbf{v}_0)\,\zeta] + \psi_x\}^k$$
$$+ \frac{\Delta t}{4}\{\epsilon\nabla\cdot[(\mathbf{v}-\mathbf{v}_0)\,\zeta] + \psi_x\}^{k-1/2}, \qquad (27a)$$

$$\zeta^{k+1} + \frac{\epsilon\,\Delta t}{2}\frac{\partial}{\partial y}(v_0\zeta)^{k+1} = L_2(\zeta^{k+1})$$
$$= \zeta^{k+1/2} - \frac{\epsilon\,\nabla t}{2}\frac{\partial}{\partial x}(u_0\zeta)^{k+1/2}$$
$$- \frac{3}{4}\Delta t\{\epsilon\nabla\cdot[(\mathbf{v}-\mathbf{v}_0)\,\zeta] + \psi_x\}^{k+1/2}$$
$$+ \frac{\Delta t}{4}\{\epsilon\nabla\cdot[(\mathbf{v}-\mathbf{v}_0)\,\zeta] + \psi_x\}^k, \qquad (27b)$$

where

$$u_0^{k+1}(x, y) = x\{u^{k+1}(1, y) - u^{k+1}(-1, y)\} + u^{k+1}(-1, y),$$

$$v_0^{k+1}(x, y) = y\{v^{k+1}(x, 1) - v^{k+1}(x, -1)\} + v^{k+1}(x, -1),$$

and

$$u^{k+1}(-1, y), \qquad u^{k+1}(+1, y), \qquad v^{k+1}(x, +1), \qquad v^{k+1}(x, -1)$$

are the known distributions of normal velocity at time step $(k+1)$ along the western, eastern, northern, and southern boundaries, respectively. In effect, this semi-implicit procedure removes and treats implicitly that portion of the advective term which arises from contributions due to nonzero normal velocities at the domain edges. The splitting of the advective term relaxes the restrictive Courant condition which arises for explicitly differenced inflow/outflow problems due to the crowding of Chebyshev collocation points near the domain boundaries.

The solution of each half step—Eq. (27a) or (27b)—proceeds similarly. Consider (27a). The implicit advective effects introduce a coupling only in the x direction. In fact, along any line $\hat{y} = \hat{y}_q$ = constant, $u_0^{k+1}(\hat{x}, \hat{y}_q)$ is at most linear in $\hat{x}$. Under these circumstances, operator $L_1(\zeta^{k-1/2})$ can be expressed spectrally as a sequence of

tridiagonal matrix equations, one for each $\hat{y}_q$ ($0 \leqslant q \leqslant N$). Similar remarks hold for operator $L_2(\zeta^{k+1})$, which is repeatedly solved along lines of constant $\hat{x} = \hat{x}_p$ ($0 \leqslant p \leqslant N$). In either case, vorticity boundary conditions are selectively introduced in place of higher-order (dynamical) equations in each tridiagonal system. Zero, one, or two vorticity conditions are imposed, depending on the corresponding number of end points of the line $\hat{x} = \hat{x}_p$ or $\hat{y} = \hat{y}_q$ which are inflow points. The resulting numerical scheme fixes the value of ζ only at inflow points; however, *all* values of boundary vorticity are in exact dynamic balance with the interior. (This is not true of either the FD or FE models—see the preceding sections.)

Once Eq. (27a) or (27b) yields $\zeta^{k+1/2}$ or ζ^{k+1}, the associated Poisson problem for the streamfunction field $\psi^{k+1/2}$ or ψ^{k+1} are solved as outlined above for a closed basin.

4. Linear and Nonlinear Box Mode Tests

In this and the following sections, we briefly describe the formulation and selected results of the prototype numerical tests mentioned in Section 1. For a more complete summary of the results, the reader is referred to Table I and Figs. 1–16. (See also Section 2.)

4.1. *Formulation*

The class of exact solutions to the linear vorticity equation ($\epsilon = 0$) satisfying homogeneous streamfunction boundary conditions on Σ are the box modes or

$$\psi(x, y, t) = \sin(\lambda x) \sin(\mu y) \cos(\lambda + t/2), \qquad 0 \leqslant x \leqslant x_B, \; 0 = y = y_B, \quad (28)$$

where x and t have been scaled with respect to d and $(\beta d)^{-1}$, respectively, and d is taken to be the scale length of the traveling wave (wavelength/2π). The parameters λ and μ, and the domain size $x_B = y_B$ are related to the integer mode numbers, m and n, by the relations

$$\lambda = m/(m^2 + n^2)^{1/2},$$
$$\mu = n/(m^2 + n^2)^{1/2},$$

and

$$x_B = y_B = \pi(m^2 + n^2)^{1/2}.$$

Given this nondimensionalization, the linear box modes have a wavelength, period, and phase speed given by 2π, 4π, and $\frac{1}{2}$, respectively. Corresponding to these physical measures are the computational measures

$$\Delta = x_B/\pi = \text{relative box size},$$
$$\nu = (N - 1)/\Delta = (N - 1)\pi/x_B = \text{spatial resolution parameter},$$

and

$$\eta = 4\pi/\Delta t = \text{temporal resolution parameter}.$$

As mentioned previously, we use N to refer to the number of spatial degrees of freedom (grid points, spectral functions, etc.) which characterizes the x and y discretization of each model.

For $\epsilon \ll 1$, we can obtain an approxomate solution to the nonlinear box mode problem using a small-amplitude expansion in ϵ. Let

$$\psi(x, y, t) = \psi_0 + \epsilon\psi_1 + \epsilon^2\psi_2 + \cdots,$$

where ψ_0 is the linear box mode solution (28). Then, to first order,

$$\nabla^2\psi_{1t} + \psi_{1x} = -J(\psi_0, \nabla^2\psi_0) \tag{29}$$

which has the solution

$$\begin{aligned}\psi_1(x, y, t) = \sin(2\mu y) \Big\{ &- \frac{\mu}{2} \sin^2 \lambda x + \frac{\lambda^2\mu}{4(1 + 2\mu^2)} \\ &\times \Big[\cos(t + 2x) - \Big(\frac{\sinh Rx}{\sinh Rx_B}\Big) \cos\Big(t + \frac{x}{2} + \frac{3x_B}{2}\Big) \\ &- \frac{\sinh R(x_B - x)}{\sinh Rx_B} \cos\Big(t + \frac{x}{2}\Big)\Big]\Big\}\end{aligned} \tag{30}$$

with

$$R = (4\mu^2 - \tfrac{1}{4})^{1/2}, \qquad \mu > \tfrac{1}{4}.$$

Taking the expansion to second order, the right-hand side of the equation for ψ_2 has a component proportional to ψ_0. This secularity destroys the uniform convergence of the approximation for large t. Following Pedlosky [33], it can be shown that by introducing the new time scale $\tau = t(1 + \epsilon^2\delta)$, all forcing terms proportional to ψ_0 can be suppressed for a suitable choice of δ. The perturbation solution $\psi = \psi_0 + \epsilon\psi_1$ can therefore be corrected by replacing t by τ in (28) and (30). The resulting expression is correct to first order; that is, its leading-order error is $O(\epsilon^2)$. Since the computed solution can be closer to (or further away from) the correct nonlinear solution than the approximate analytical solution, the RMS error is an unknown mix of errors in both the computed and approximate solutions.

4.2. *Finite-Difference Model Results*
(*Table* I, *Cases* 1–9; *Figs.* 1–6)

An exact solution, ψ_d, to the discrete finite-difference equations (5a) and (5b) can be found by assuming

$$\psi_d(x, y, t) = \sin(\lambda x) \sin(\mu y) \cos(\alpha x + \sigma t), \tag{31}$$

where α and σ are, in general, functions of the nondimensional space and time increments h and Δt. (We therefore assume that the discrete and analytic results

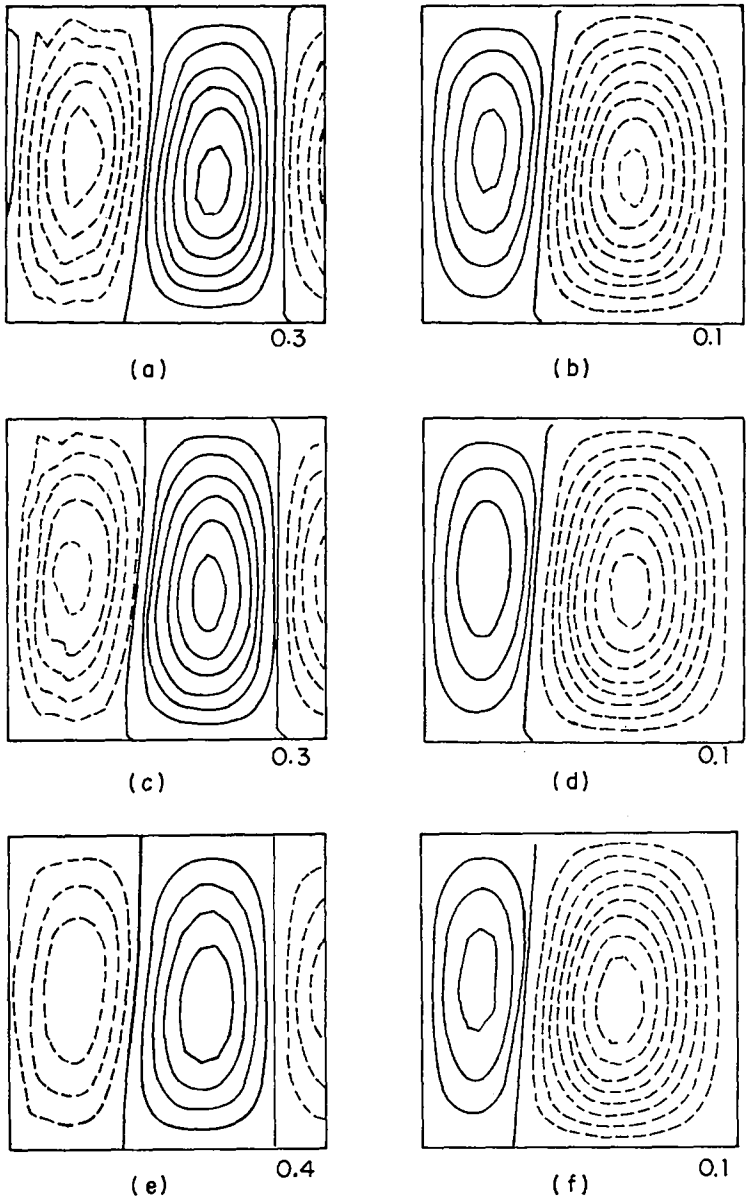

FIG. 4. Nonlinear box mode solution at $t = 5$ periods with $(\nu, \eta, m, n, \epsilon) = (16(2)^{1/2}, 64, 1, 1, 0.2)$. (a, b), (ζ, ψ): FD model, CI = (0.3, 0.1); (c, d), (ζ, ψ): FE model, CI = (0.3, 0.1); (e, f), (ζ, ψ): PS model, CI = (0.4, 0.1).

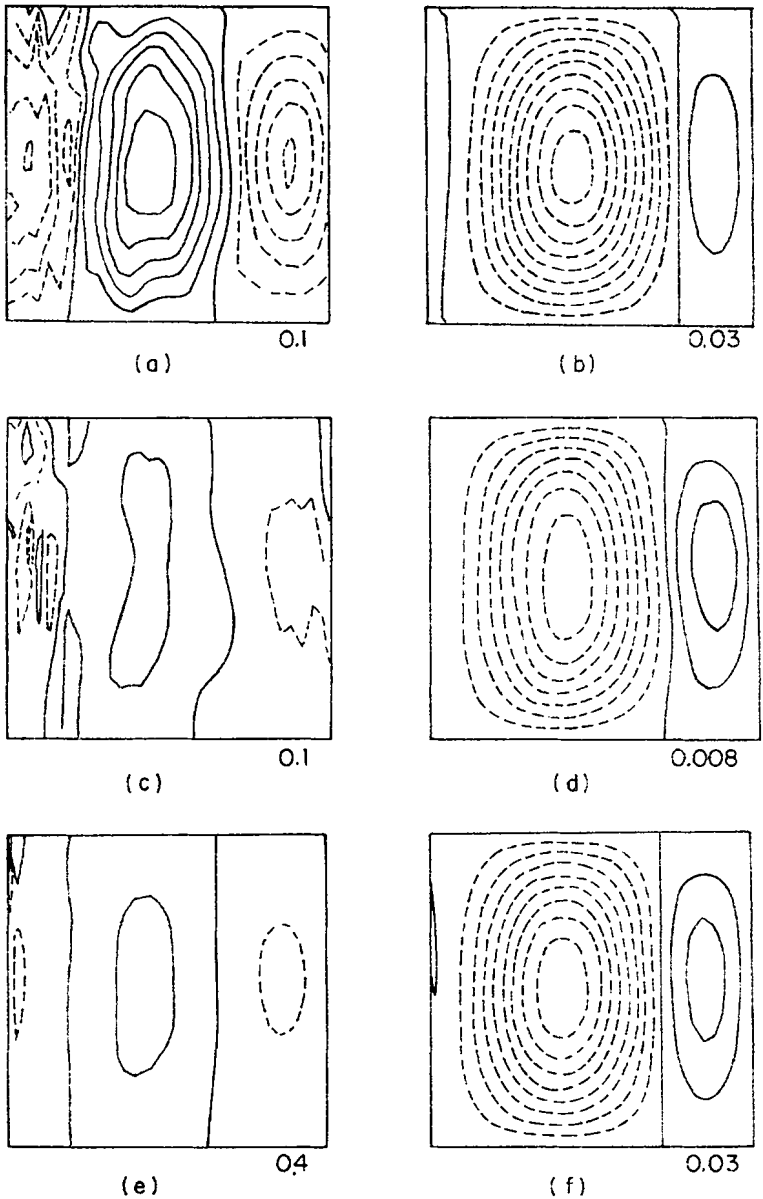

FIG. 5. As Fig. 4. (a, b), (ζ', ψ'): FD model, CI = (0.1, 0.03); (c, d), (ζ', ψ'): FE model, CI = $(0.1, 8.0 \times 10^{-3})$; (e, f), (ζ', ψ'): PS model, CI = (0.4, 0.03).

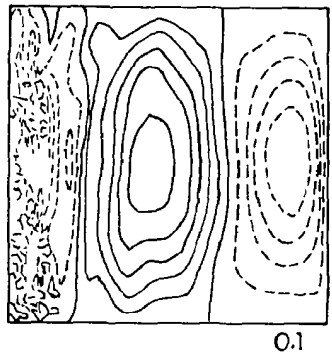

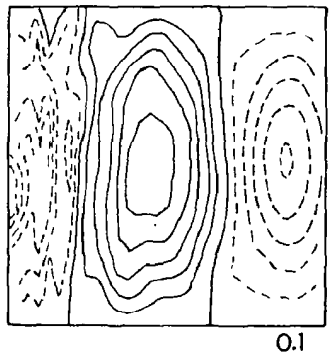

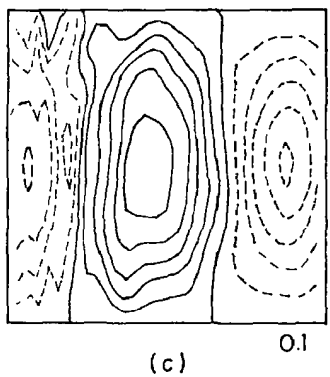

FIG. 6. As Fig. 4, CI = 0.1. (a), ζ': FD model, $\zeta_\Sigma = \zeta_a$; (b), ζ' : FD model, ζ_Σ specified by Kreiss condition; (c), ζ' : FD model, ζ_Σ specified by Sundstrom/Davies condition.

differ only in the wavelength and phase speed of the traveling component of the box mode.) Substituting in the trial solution (31), we find that

$$\sin(\sigma\,\Delta t) = 1/2h\,\Delta t$$

and

$$\cos(\alpha h) = \frac{\cos h(\lambda h)}{2 - \cos(\mu h)}.$$

For $h \ll \pi$ and $\Delta t \ll \pi$,

$$\alpha = 1 - \frac{\mu^2}{12}(2 + \mu^2)\,h^2 + O(h^4)$$

and

$$\sigma = 1/2 + 1/48\,\Delta t^2 - 1/24(4 - 2\mu^2 - \mu^4)\,h^2 + O(\Delta t^4 + h^4).$$

That this is indeed the correct computational result has been verified by direct numerical integration of the finite-difference equations (5a) and (5b). The resulting computational solution differs from (31) only due to machine truncation error—that is, $\mathrm{RMS}(\zeta') = \mathrm{RMS}(\zeta_c - \zeta_d) = O(10^{-11})$.

In comparison to the analytic solution (for which $\alpha = 1$ and $\sigma = \frac{1}{2}$), the wavelength and period are correct only to second order in space and time. For sufficiently small phase errors ϕ ($=\sigma_a - \sigma_d$), it is easy to show that

$$\mathrm{RMS}(\psi') = [2(1 - \cos\phi t)]^{1/2}.$$

The initial error growth rate

$$\mathrm{RMS}(\psi') \simeq \phi t + O(\phi t)^3 \tag{32}$$

is therefore linear in time with a slope given by

$$\begin{aligned}\phi &= (1/48)\,\Delta t^2 - 1/24(4 - 2\mu^2 - \mu^4)\,h^2 \\ &\simeq (\pi^2/3)\,\eta^{-2} - \pi^2/24(4 - 2\mu^2 - \mu^4)\,\nu^{-2}.\end{aligned} \tag{33}$$

An example of this behavior is given in Figs. 3a and b for $(\nu, \mu, m, n) = (16(2)^{1/2}, 128, 1, 1)$.

Note that for the discrete finite-difference solution, the spatial and temporal contributions to the phase error ϕ, being of opposite sign, tend to offset each other. Because of this compensation effect, if an optimal choice of Δt and h is made, the total error of the finite-difference scheme can be made quite small although the contributions to ϕ from spatial and temporal error are individually large. This property explains the computed results as functions of ν ($\simeq\pi/h$) and η ($=4\pi/\Delta t$) in which increasing η (holding ν fixed), and vice versa, can increase, rather than decrease the error of the computed finite-difference solution. Compare, for instance, Table I, cases 2 and 3.

For $\epsilon > 0$, the values of ζ on the boundary enter the problem through the nonlinear terms. Three ways of fixing ζ_Σ have been examined in the context of the finite-difference model. They are the specification of the analytic value of the vorticity ($\zeta_\Sigma = \zeta_a$), and the Kreiss and Sundstrom/Davies conditions—see Section 3. For the nonlinear box mode problems studied, the following behavior was noted.

4.2.1. $\epsilon = 0.2$

For low to moderate Rossby number the FD model is always well behaved out to at least $t = 5$ periods independent of computational boundary condition. When $\zeta_\Sigma = \zeta_a$ is the required condition, however, there is a buildup of small-scale perturbation vorticity on the western wall—Fig. 6a. (Since similar effects are noted in all the models, this buildup is presumably a manifestation of the physical response of the system to the presence of small-scale numerical truncation error.) This accumulation of ζ' is less rapid when the Kreiss boundary condition is applied everywhere (Fig. 6b) and is nearly eliminated when the Sundstrom/Davies condition is invoked (Fig. 6c). The RMS error measures are, however, comparably large—several tens of percentage after five periods—for all three boundary conditions (Table I, case 6).

4.2.2. $\epsilon = 0.4$

For higher Rossby number, the error accumulation to the west is much more rapid and becomes noticeable in even the Sundstrom/Davies experiments. In contrast to the finite-element and spectral models, however, the finite-difference scheme does not suffer catastrophic numerical instability when grid-scale vorticity begins to accumulate. This lower sensitivity to the presence of small-scale vorticity is perhaps due to a small amount of (numerical) dissipation implicit in the finite-difference formalism. In general, the RMS error quantities have a linearly increasing trend similar to, but somewhat greater than, that noted for $\epsilon = 0$. Some of this increased error is attributable to the approximate nature of our reference solution.

4.3. *Finite-Element Model Results*

(*Table* I, *Cases* 1–9; *Figs.* 1–5)

The following functional dependence on the parameters ν and η has been noted in the error analysis of the finite-element model results.

4.3.1. $\epsilon = 0$, $\eta \ll 4(2)^{1/2}\nu$

For relatively coarse temporal resolution, the RMS error quantities are well described, as in the finite-difference and spectral models, by the relation $\phi \simeq (\pi^2/3)\,\eta^{-2}$ and consequently by an initial linear increase with time proportional to η^{-2}. This reflects the fact that for sufficiently large ν the error is attributable to temporal truncation effects (identical in all three models).

4.3.2. $\epsilon = 0$, $\eta \simeq 4(2)^{1/2}\,\nu$

As η increases, RMS(ζ') for the finite-element is characterized by a large initial value followed by a very slow linear increase thereafter (Fig. 3c). (RMS(ψ')—whose values are perhaps dictated by a different mechanism than those of RMS(ζ')—maintains a linear trend.) Apparently, the spatial contribution to the phase error ϕ is of a form quite different than that implied by (33). For one thing, we know the phase error to be proportional to h^4 for the linearized advectvie equation [25]. In parameter ranges where this diminished error growth rate prevails, the finite-element model may offer some advantages for long-term calculations; however, we have not verified this possibility.

For $\epsilon = 0$, the maximum pointwise errors in vorticity tend to be near the western boundary, but there is very little preferential accumulation of small-scale vorticity there. With nonlinearity ($\epsilon > 0$), the situation is qualitatively different in the following way(s).

4.3.3. $\epsilon = 0.2$

With $\epsilon = 0.2$ an initial eastern boundary layer is generally observed in the field of ζ'. This boundary layer eventually disappears, to be replaced by an accumulation of perturbation vorticity on the western wall, as in the FD and PS simulations (Fig. 5c). In other respects, the solutions bear some resemblance to those for $\epsilon = 0$. RMS(ζ') again shows evidence for certain values of ν and η of leveling off with time after an initially large increase, and ψ' sometimes resmebles a box mode (out of phase with the reference solution).

4.3.4. $\epsilon = 0.4$

With stronger nonlinearity, perturbation vorticity on the grid-point scale collects first on the western wall and then in the center of the domain (perhaps as a numerical response to insufficient resolution of the narrow wall layers of ζ'). Once this stage is reached, the solution becomes numerically unstable, typically after about five periods (Table I, case 7).

This catastrophic effect of small-scale vorticity accumulation is reached in less than a period for $\epsilon \sim 0.8$.

4.4. *Pseudospectral Model Results*
(*Table* I, *cases* 1–9; *Figs.* 1–5)

For linear box modes, for which we have the analytic solution, the spectral model shows three distinct types of behavior corresponding to different regimes in the space of the nondimensional computational parameters.

4.4.1. $\epsilon = 0$, $\eta \ll 16(2)^{1/2}\,\nu$

Quite a large range of ν exists for which spatial truncation errors are totally insignificant in comparison to those arising from time-differencing. For this range of

parameters, the RMS quantities grow linearly in time (Figs. 3e and f) and can be quantitatively explained by the simple phase error analysis of Section 4.2 if, in addition, the assumption is made that $h \simeq 0$. There is no apparent buildup of perturbation vorticity at scales other than those of the box modes themselves. Since the computational errors are due to time-differencing alone, they are proportional to η^{-2}—see Table I, cases 1 and 2.

4.4.2. $\epsilon = 0$, $\eta \simeq 16(2)^{1/2}\,\nu$

For $\nu \simeq 4$ and standard values of η (=64 or 128), spatial error becomes noticeable. The growth of the RMS quantities is no longer strictly linear. In fact, the temporal variation of RMS(ζ') begins to assume characteristics noted (over a larger range of ν and η) in the finite-element model: a large initial error growth, followed by a relatively slow increase with time. Indeed, it is interesting to note that the spectral model can show the effects of compensating space- and time-differencing errors, which is a general property of the finite-difference model. Something of this kind is clearly happening in the spectral model when, for instance, RMS(ψ') decreases when the box mode numbers $m = n$ are increased from 2 to 3 at constant ν and η (Table I, cases 4 and 5). For these values of ν, perturbation vorticity does appear to collect on the western wall, perhaps in scales much smaller than those of the original box modes.

4.4.3. $\epsilon = 0$, $\eta \gg 16(2)^{1/2}\,\nu$

As expected, for extremely small values of the resolution parameter ν, substantial spatial error results. The RMS error quantities once again grow in a quasi-linear fashion. The perturbation vorticity field is now dominated by a narrow layer on the western wall. The amplitude of this feature is sufficiently large (after 10 periods) to contribute recognizably to the total vorticity field.

For the nonlinear box modes, behavior of the computational system depends sensitively on ϵ in the following manner.

4.4.4. $\epsilon = 0.2$

For $\epsilon \lesssim 0.2$, the spectral model is well behaved out to $t \simeq 5$ periods. By this time, however, integrated $|\nabla\zeta|^2$ has begun to increase rapidly. Significantly longer integrations could therefore be expected to suffer eventual computational instability. Even at this level of nonlinearity, increasing ν and or η (over the range tested: $\nu = 8(2)^{1/2}$, $\eta = 128$) does nothing to improve the error measures (Table I, cases 6, 8, 9). The manifestation of error growth is a very definite pereferential accumulation of perturbation vorticity in narrow layers adjacent to the western wall of the domain (Fig. 5e). This accumulation of perturbation vorticity may ultimately result from local numerical truncation errors which are propagated to the west where, in the absence of dissipation, they collect in a narrow boundary layer.

4.4.5. $\epsilon = 0.4$

The results for $\epsilon = 0.4$ are much more catastrophic, with perturbation vorticity collecting so quickly on the western wall that locally intense gradients of vorticity

grow to destroy the calculation after only 2.5 periods (Table I, case 7). This behavior is once again independent of ν and η. When the calculations go bad, they do so very quickly; presumably the computed fields are still quite accurate up to the instant of catastrophic failure. (This essentially instantaneous instability is a feature of the FE model also.) In a related calculation, it has been shown that the useful integration of the spectral model can be prolonged to $t = 5$ periods (and beyond) by periodically filtering the vorticity field by setting

$$b^k_{nm}(\text{filtered}) = f_n f_m b^k_{nm}$$

(see Section 3.3), where the spectral filter

$$f_n = 1.0 - \exp\{-\mathscr{H}(N^2 - n^2)\}$$

and $\mathscr{H}$ is adjusted so that ζ^k is smoothed only at the highest wavenumbers. By comparing the filtered and unfiltered results, it is known that such filtering does not affect the large-scale features of the circulation and that the two streamfunction fields (up to the moment of instability in the unfiltered calculation) are virtually identical (an example is given in Fig. 13, Section 6).

Lastly, it is important to note that the RMS error quantities for the nonlinear box mode problems are nearly independent of ν and η. If there is nothing idiosyncratic about these problems, then we must conclude that the largest contribution to the RMS error fields comes from the uncertainty in the exact analytic solution to the nonlinear box mode problem.

4.5. *Intercomparison*

Results from the linear box mode tests (see Table I) demonstrate that the finite-element (with $N = 33$) and pseudospectral (with $N = 17$) models are comparably accurate over the range of ν and η studied. (The spectral model is, however, somewhat more efficient—Table II.) And, even though the finite-difference is by far the least accurate model, a phase error analysis of the FD model results shows that errors can be minimized for optimal choices of ν and η. Since these optimal parameters are functions of the time and space scales of the problem, however, this property will be of questionable value in more general problems characterized by multiple time and space scales. Even if a degree of compensation could be guaranteed in a specific problem, errors get smaller only if ν and η are increased in the same ratio. A fourfold decrease in the RMS errors would therefore require η and ν to be simultaneously increased by a factor of 2, with a resulting increase in computational work of a factor of 8. In contrast, the spectral model, and to a lesser extent the FE model, generally require only η to be increased—say by 2, for a fourfold reduction in error—because of their much greater spatial accuracy.

In the case of the nonlinear box modes, interpretation of the results is compilcated by the fact that we have only a perturbation solution with which to compare the

TABLE II

Approximate Model Running Times as Functions of N (CPU Time in Seconds on the NCAR CDC 7600 per 100 Time Steps)

	Linear Rossby waves			Nonlinear Rossby waves		
N	FD	FE	PS	FD	FE	PS
17	1.5	3.1	3.7	2.0	3.4	12.1
33	6.3	13.1	10.6	8.3	14.0	31.1
33:17	4.2	4.2	2.9	4.2	4.1	2.6

[a] The ratios of the running times (also listed) indicate that the computational time increases as approximately N^2 for the FD and FE models and as $N \ln N$ for the PS model. Running times for the other linear and nonlinear model problems are comparable to those quoted here for the Rossby wave calculations.

computational results. Consequently, our error measures—such as RMS(ψ'), etc.—reflect three sources of error: spatial and temporal truncation errors, and the error associated with not knowing the exact analytic solution. The RMS quantities listed in Table I for the nonlinear box mode tests cannot be used as direct measures of model performance.

The essential *qualitative* distinction that can be made between the results of the three models for $\epsilon > 0$ is that the finite-difference model, though presumably less accurate, appears not to be susceptible to catastrophic numerical instability when small-scale error fields are present. Under these conditions, the FD spatial truncation error is, however, formally quite large. A nonlinear FD solution will therefore become invalid after only a short period of time even though a stable calculation can be maintained for a much longer time.

5. Forced Nonlinear Box Mode Tests

5.1. *Formulation*

One means of avoiding the complications associated with having only a perturbation solution to the nonlinear box mode problem is to consider the analogous forced problem, that is, to seek solutions to the inhomogeneous equation

$$\frac{\partial}{\partial t} \nabla^2 \psi + \epsilon J(\psi, \nabla^2 \psi) + \psi_x = F(x, y, t), \tag{34}$$

where F is some suitably chosen forcing function. As before, ψ is required to vanish on Σ. In particular, we wish to examine solutions with spatial and temporal characteristics similar to those of the linear box modes. Accordingly, set

$$\psi_a(x, y, t) = \sin x \sin y \cos(ax + by + ct), \qquad 0 \leqslant x, y \leqslant \pi, \tag{35}$$

where a, b, and c are arbitrary constants which determine the wavelength, period, and phase speed of the forced mode ($2\pi/(a^2 + b^2)^{1/2}$, $2\pi/c$, and $c/(a^2 + b^2)^{1/2}$, respectively). This will be a solution to (34) so long as

$$F(x, y, t) = \left\{\frac{\partial}{\partial t}\nabla^2 + \epsilon J(\psi_a, \nabla^2) + \frac{\partial}{\partial x}\right\}\psi_a(x, y, t), \tag{36}$$

which will in general be nonvanishing, as will $J(\psi_a, \nabla^2\psi_a)$. Given specific values of parameters a, b, c, and ϵ, the functional form of F can therefore be directly calculated. For the following tests, the Rossby number has been fixed at $\epsilon = 0.2$. An examination of higher ϵ behavior is reserved for the open boundary calculations of Section 6.

5.2. *Finite-Difference Model Results*

(*Table* I, *Cases* 10–12; *Figs.* 7–9)

Table I shows the RMS error measures for the finite-difference model after two periods for a variety of values of ν and η. The results indicate that the FD error norms are in general somewhat smaller than those for the linear box mode problems with comparalbe nondimensional parameters. Compare Figs. 3a and b and 9a and b, for instance. In addition, a partial compensation between spatial and temporal errors once again exists so that the RMS errors (as in the linear box mode cases) need not decrease with increasing η and ν (Table I, cases 11 and 12). As in the nonlinear box mode problems, perturbation vorticity tends to collect on the western boundary (Fig. 8a). This appears to eb a quite general property of all the simulations when $\epsilon \neq 0$, regardless of the orientation of the forced mode.

5.3. *Finite-Element Model Results*

(*Table* I, *Cases* 10–12; *Figs.* 7–9)

The FE model behaves similarly, yielding very accurate and stable solutions for a range of parameters (Table I, cases 10–12). For instance, with $(\nu, \eta, a, b) = (32, 128, 1/2^{1/2}, 1/2^{1/2})$ the RMS errors are $O(1\text{–}2\,\%)$ after two periods. As in the FD, and as we shall see, the spectral computations, the RMS errors given by the FE solution to the nonlinear forced box mode problem are typically no less, and very often several times smaller, than the errors noted for the linear unforced box mode tests with comparable resolution. Figures 3c and d and 9c and d give an example of this behavior. (Note also that the character of the RMS error curves seems to be modified by the forcing such that RMS(ζ') is now a quasi-linear function of time over the range of parameters examined here.) The perturbation fields associated with the forced problems, although small in amplitude, are still characterized by small-scale, westward-trapped ζ' and large-scale ψ' patterns (Fig. 8).

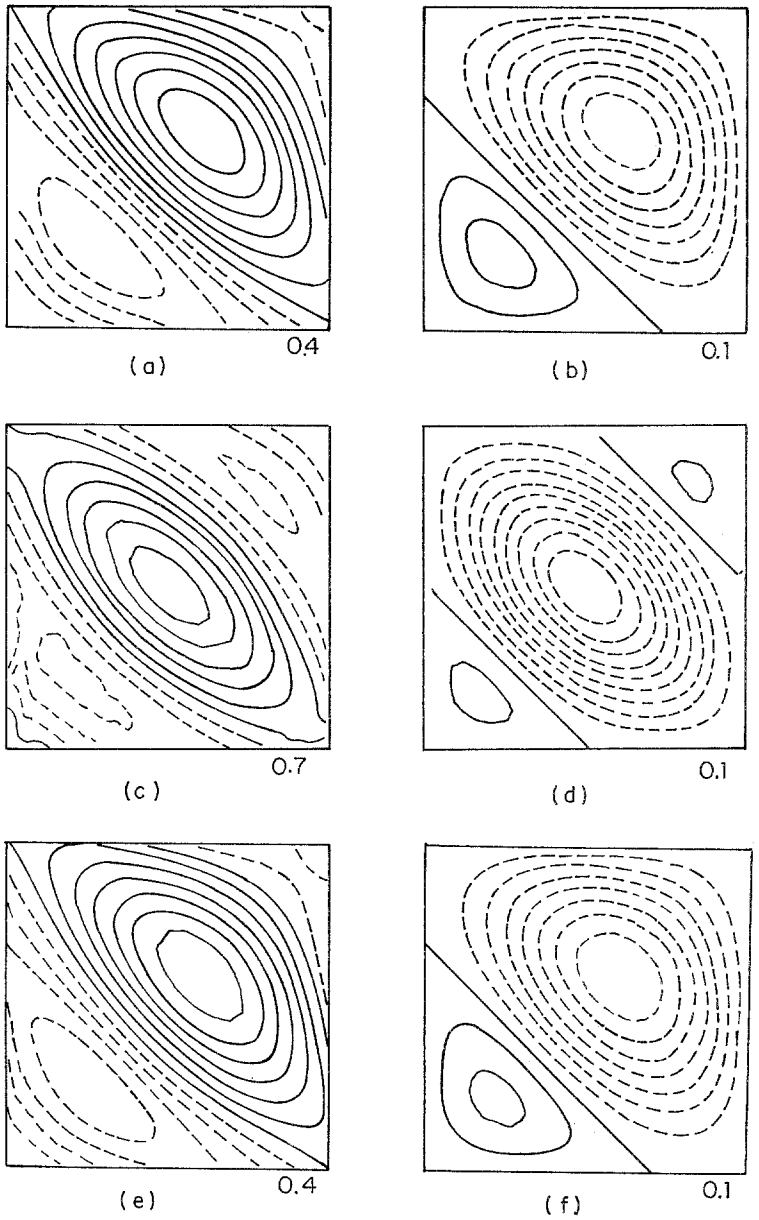

FIG. 7. Forced nonlinear box modes with $(\nu, \eta, a, b, \epsilon) = (32, 128, 1/2^{1/2}, 1/2^{1/2}, 0.2)$. (a, b), (ζ, ψ): FD model, $t = 2$ periods, CI = (0.4, 0.1); (c, d), (ζ, ψ): FE model, $t = 5$ periods, CI = (0.7, 0.1); (e. f), (ζ, ψ): PS model, $t = 5$ periods, CI = (0.4, 0.1).

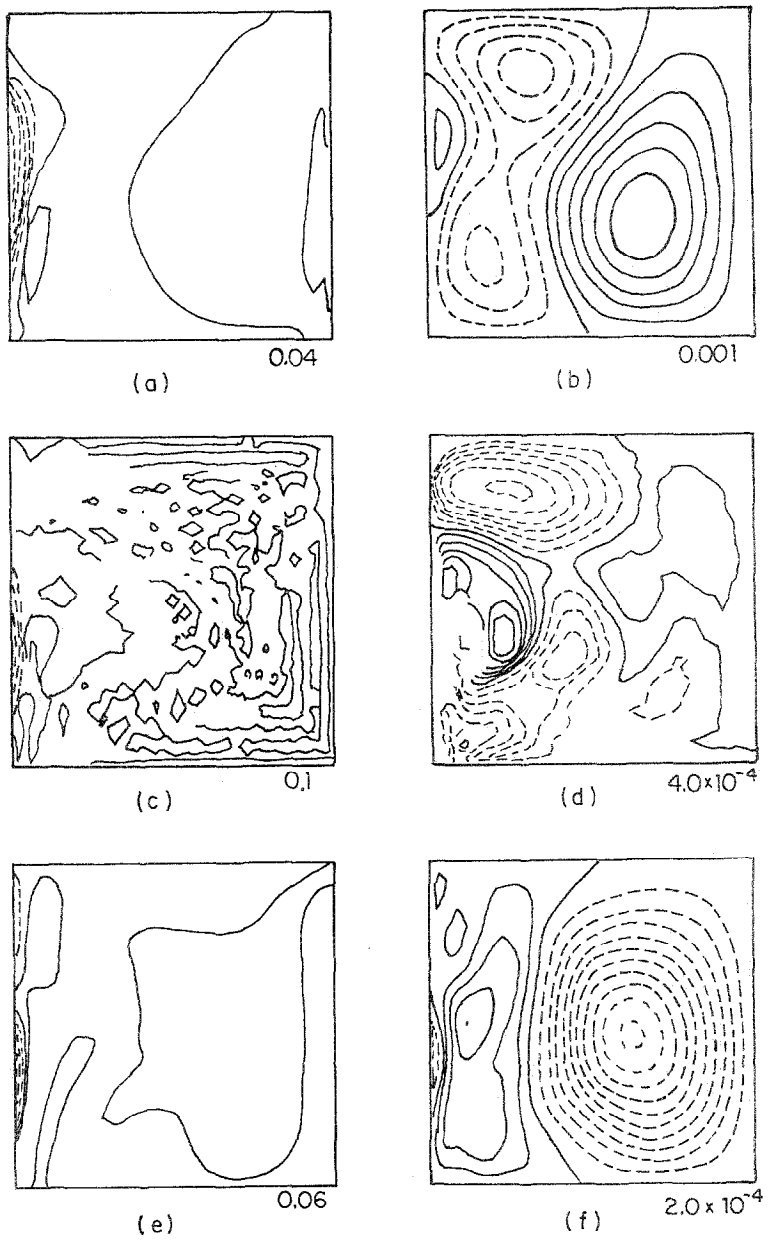

FIG. 8. As Fig. 7. (a, b), (ζ', ψ'): FD model, $t = 2$ periods, CI $= (0.04, 1.0 \times 10^{-3})$; (c, d), (ζ', ψ'): FE model, $t = 5$ periods, CI $= (0.1, 4.0 \times 10^{-4})$; (e, f), (ζ', ψ'): PS model, $t = 5$ periods, CI $= (0.06, 2.0 \times 10^{-4})$.

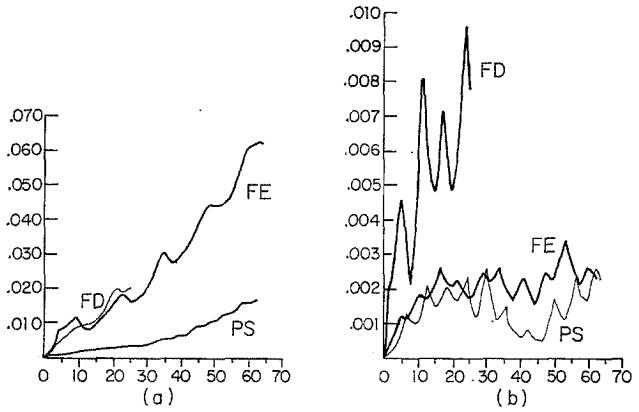

FIG. 9. As Fig. 7. (a, b); RMS(ζ', ψ'): FD model, $0 \leqslant t \leqslant 2$ periods; FE model, $0 \leqslant t \leqslant 5$ periods; PS model, $0 \leqslant t \leqslant 5$ periods.

5.4. *Pseudospectral Model Results*
(*Table* I, *Cases* 10–12; *Figs.* 7–9)

These calculations were all performed with very high spatial resolution ($\nu \geqslant 16$); consequently, insignificant spatial truncation error is expected. With a diagonally propagating mode ($a = b = 1/2^{1/2}$) and $\eta = 128$, the RMS errors are in fact very small, being no more than 0.5 % after five periods of integration. Reference to Table I and Figs. 9e and f demonstrates, however, that not only are the RMS errors no longer strictly proportional to η^{-2}—as they were in the unforced case with sufficient spatial resolution—but the error trends are not linear in time. Although RMS(ζ') increases monotonically, RMS(ψ') seems to vary quasi-periodically with little superimposed trend (Figs. 9e and f).

As in the FD and FE simulations, the PS results for the forced nonlinear box mode problems show a similar tendency for small-scale ζ' to accumulate at the western edge of the domain (Fig. 8e). The rate of this error accumulation might plausibly be thought to increase dramatically with ϵ, as in the nonlinear box mode problems; however, this hypothesis was not tested.

None of these conclusions depend sensitively on the direction of propagation of the forced model.

5.5. *Intercomparison*

All three models are capable of delivering an accurate and stable solution to the forced nonlinear box mode problem for the computational parameters considered here. In all cases, the observed RMS errors are less than or equal to those noted in the linear box mode cases (for comparable ν and η). It is quite likely that this reduction in numerical error, despite going to a problem with nontrivial nonlinearities, is in some sense associated with a "locking in" of the numerical solution to the applied

forcing. The quasi-oscillatory nature of the resultant RMS(ψ') error curves—see especially Fig. 9f—argues for such a process.

6. Linear and Nonlinear Rossby Wave Tests

6.1. *Formulation*

The advected Rossby wave

$$\psi(x, y, t) = -\gamma y - \sin(kx + ly + \omega t), \tag{37}$$

where

$$\omega = k(1 - \epsilon\gamma) \tag{38}$$

and

$$k^2 + l^2 = 1,$$

is a solution to both the linear and nonlinear vorticity equations (3). As for the box modes, we have scaled with respect to $d = (2\pi)^{-1}$ times the wavelength of the traveling wave; u_0, a characteristic particle velocity; and the time scale $(\beta d)^{-1}$. In the resulting nondimensional system, the wavelength is 2π, and the basin size $x_B = \pi\Delta$, where Δ is the number of half wavelengths per box width (a measure of the structure of the solution). Theoretically it is known that Rossby waves are individually unstable to small perturbations [34] with an e-folding time proportional to $(\epsilon)^{-1}$. This growth time scale is comparable in all cases to the entire duration of the experiment. Due to the absence of large-amplitude perturbations (or "noise") that can efficiently extract energy from the primary wave, it is cunlikely that purely physlia instabilities—as opposed to computational ones—play a role in the following results. The reader should note that the nonlinearity of these model problems is trivial (that is, self-canceling) when $\gamma = 0$.

6.2. *Finite-Difference Model Results*
(*Table* I, *Cases* 13–28; *Figs.* 10–12, 14–16)

The results for one linear Rossby wave experiment in which $(\nu, \eta, \epsilon) = (32/3.5, 128, 0)$ are listed in Table I, case 13. Variations in the RMS error measures as functions of ν and η did not differ from the comparable dependencies noted for the linear box modes—see Section 4.5—and hence will not be reiterated here. The one substantive difference between these and the other linear problems is that RMS(ψ') and RMS(ζ') are not strictly linear in time but appear to be leveling off at $t = 5$ periods.

With no mean flow and moderate nonlinearity, $(\epsilon, k, l, \gamma) = (0.4, 3/13^{1/2}, 2/13^{1/2}, 0)$, the RMS errors of the FD simulations are characterized by very small temporal, relative to spatial, errors. At the pivotal resolution $(\nu, \eta) = (32/3.5, 64)$,

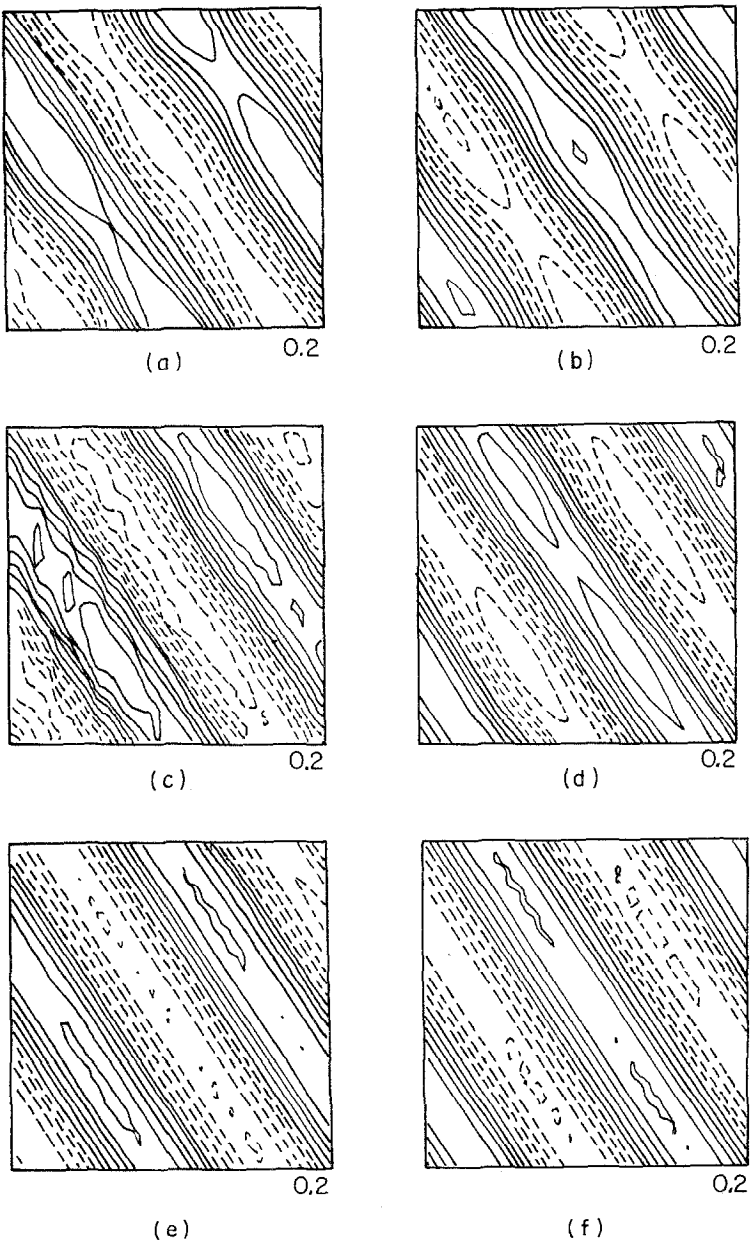

FIG. 10. Nonlinear Rossby waves at $t = 5$ periods with $(\nu, \eta, k, l, \epsilon, \gamma) = (32/3.5, 64, 3/13^{1/2}, 2/13^{1/2}, 0.4, 0.0)$. (a, b), (ζ, ψ): FD model, CI = (0.2, 0.2); (c, d), (ζ, ψ): FE model, CI = (0.2, 0.2); (e, f), (ζ, ψ): PS model, CI = (0.2, 0.2), filtered.

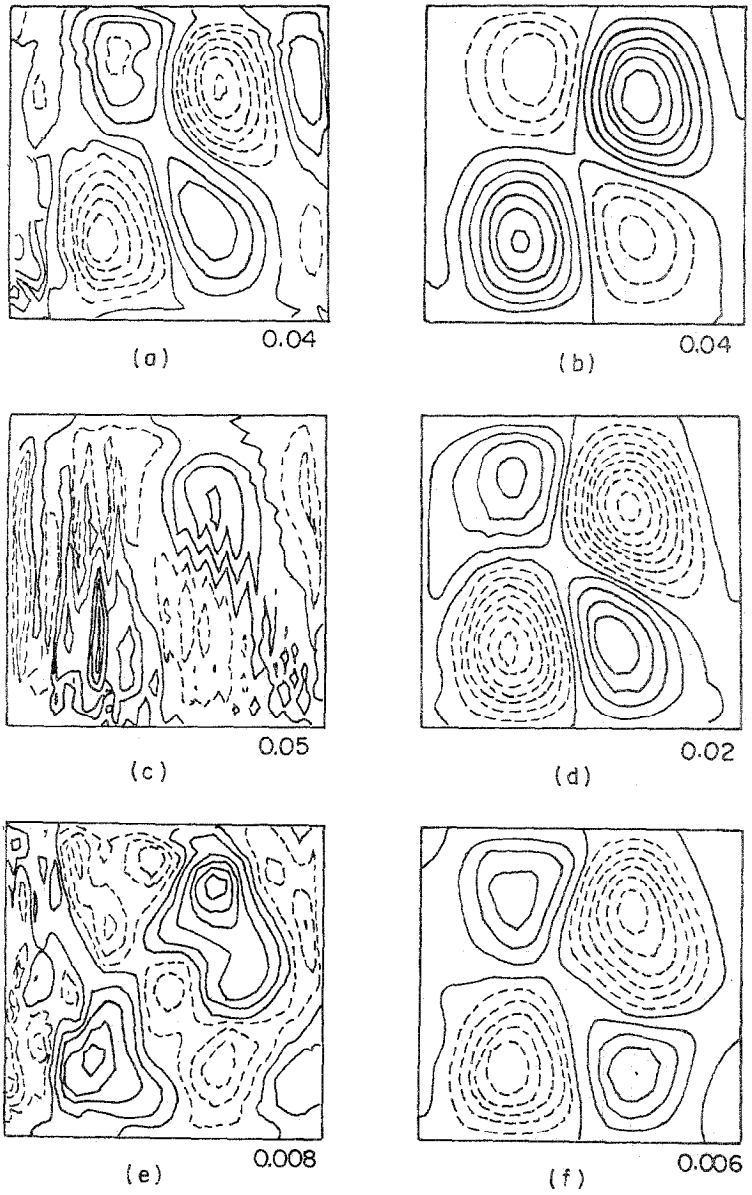

FIG. 11. As Fig. 10. (a, b), (ζ', ψ'): FD model, CI = (0.04, 0.04); (c, d), (ζ', ψ'): FE model, CI = (0.05, 0.02); (e, f), (ζ', ψ'): PS model, CI = (8.0×10^{-3}, 6.0×10^{-3}), filtered.

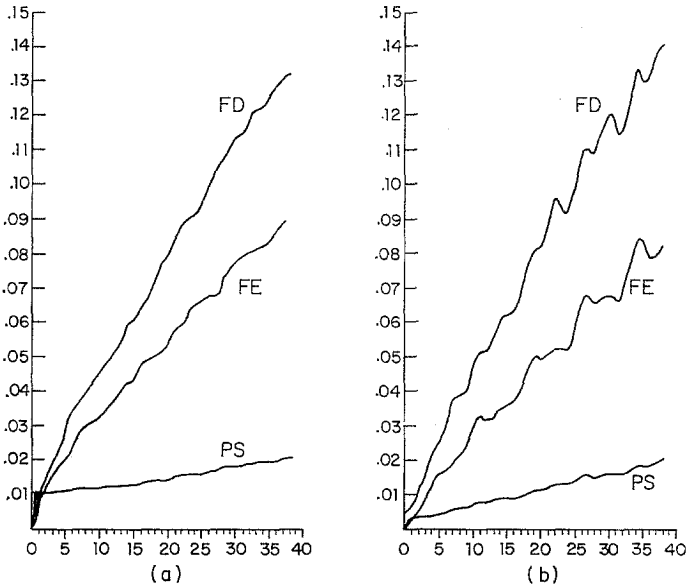

FIG. 12. As Fig. 10, $0 \leqslant t \leqslant 5$ periods. (a, b), RMS(ζ', ψ'): FD model; FE model; PS model, filtered.

RMS(ψ') $\simeq$ RMS(ζ') $\simeq$ NDIF(NRG) = $O(14\,\%)$ after five periods. The manifestation of error in these simulations are perturbation fields closely resembling box modes which begin to destroy the plane wave nature of the solution after a few periods (Figs. 10a,b and 11a,b). This form for the error fields appears to be independent of ν and η. Their amplitude, as stated previously, depends sensitively on ν but not on η for those values considered here. (In addition, other simulations—cases 16, 20, and 22—show that RMS(ψ') and RMS(ζ') also depend on the orientation of the reference wave so that cancellation of time and space errors can sometimes occur.) The RMS error measures typically grow quasi-lineary—e.g., see Figs. 12a,b—though in some cases there is a tendency for the rate of error growth to slow toward the end of the simulation. Lastly, the change in the integrated kinetic energy of the system is $O(-10\,\%)$, somewhat larger than that observed in the nonlinear box mode problems for comparable ν and η.

For $\epsilon = 0.8$ and $(\nu, \eta, k, l, \gamma) = (32/3.5, 128, 3/13^{1/2}, 2/13^{1/2}, 0)$, the same qualitative remarks apply. The field of ζ' does, however, begin to show some noticeable grid-scale variability in comparison to its rather smooth modelike appearance for $\epsilon = 0.4$. The associated values of RMS(ψ') and RMS(ζ') are comparable to those for $\epsilon = 0.4$.

With the addition of a mean flow ($\gamma \neq 0$), the FD model actually becomes more accurate, perhaps reflecting the increased smoothness of the ψ field (Fig. 14b). With $\gamma = 0.5$, the FD model delivers a stable solution with an accuracy of $O(20\,\%)$ in vorticity, but only $O(3$–$4\,\%)$ in both streamfunction and energy (Table I, case 17).

For a mean flow of the opposite sense ($\gamma = -0.5$), the errors are comparable or [illegible] fields of ψ' and ζ' are dominated by large-scale box modelike features. Similar remarks hold for Rossby waves of different orientation.

6.3. *Finite-Element Model Results*

(*Table* I, *Cases* 13–28; *Figs.* 10–12, 14–16)

The results of the FE linear Rossby wave calculations are as expected from Sections 4.3 and 6.3. With $(\nu, \eta, k, l, \gamma) = (32/3.5, 128, 3/13^{1/2}, 2/13^{1/2}, 0)$, $\mathrm{RMS}(\psi') \lesssim \mathrm{RMS}(\zeta') \lesssim O(1\,\%)$ at the end of five periods of integration (Table I, case 13). In fact, $\mathrm{RMS}(\zeta')$ has nearly stopped increasing altogether, though $\mathrm{RMS}(\psi')$ continues to rise quasi-linearly. Associated with these error levels are fields of ψ' and ζ' composed of [illegible] field. Errors in the vorticity are resident at somewhat smaller scales. Consider, for instance, Figs. 10c,d and 11c,d, which show the total and perturbation fields, respectively, at the end of a five-period integration with $(\nu, \eta, \epsilon, k, l, \gamma) = (32/3.5, 64, 0.4, 3/13^{1/2}, 2/13^{1/2}, 0)$. For this case, the FE model has errors of $O(9\,\%)$, a significant improvement over the second-order FD results which, as remarked, have a large component of spatial truncation error. On the contrary, the FE errors are most sensitive to changes in η, at least in the parametric neighborhood of our pivotal calculation (Table I, cases 14–16).

Quantitatively similar statements can be made for simulations at higher Rossby number – case 19, $\epsilon = 0.8$—and in the presence of mean advection—cases 17 and 18, $\gamma = -0.5$. (Note that the latter differ from the nonadvected Rossby waves in that they have nontrivial nonlinearities.) As with the FD model, neither the increase in ϵ nor the inclusion of mean advection seriously increases the RMS errors of the FE model. As a result, for constant ν and η (spatial and temporal resolution), $\mathrm{RMS}(\psi') = O(1\text{–}4\,\%)$ and $\mathrm{RMS}(\zeta') = O(3\text{–}10\,\%)$ after five periods (Table I, cases 16–19). The error growth is quite consistently nearly linear (Figs. 16c,d) with the perturbation streamfunction appearing at the largest (basin) scales although in a somewhat less organized pattern than the box modelike features noted with $(\epsilon, \gamma) = (0.4, 0)$—Figs. 11d and 15d.

6.4. *Pseudospectral Model Results*

(*Table* I, *Cases* 13–28; *Figs.* 10–16)

For $0.4 \lesssim \epsilon \lesssim 0.8$, the spectral model suffers eventual numerical instability at some $t = 5$ periods. Figure 13a shows a typical example where $(\nu, \eta, \epsilon, \gamma) = (16/3.5, 128, 0.4, 0)$. By $t = 1.5$ periods, the total vorticity is dominated by small-scale noise; catastrophic failure of the numerical experiment occurs shortly thereafter. The most intense grid-scale vorticity features occur at one or more points on the boundary, but the noise is also substantial in the interior along a line normal to that

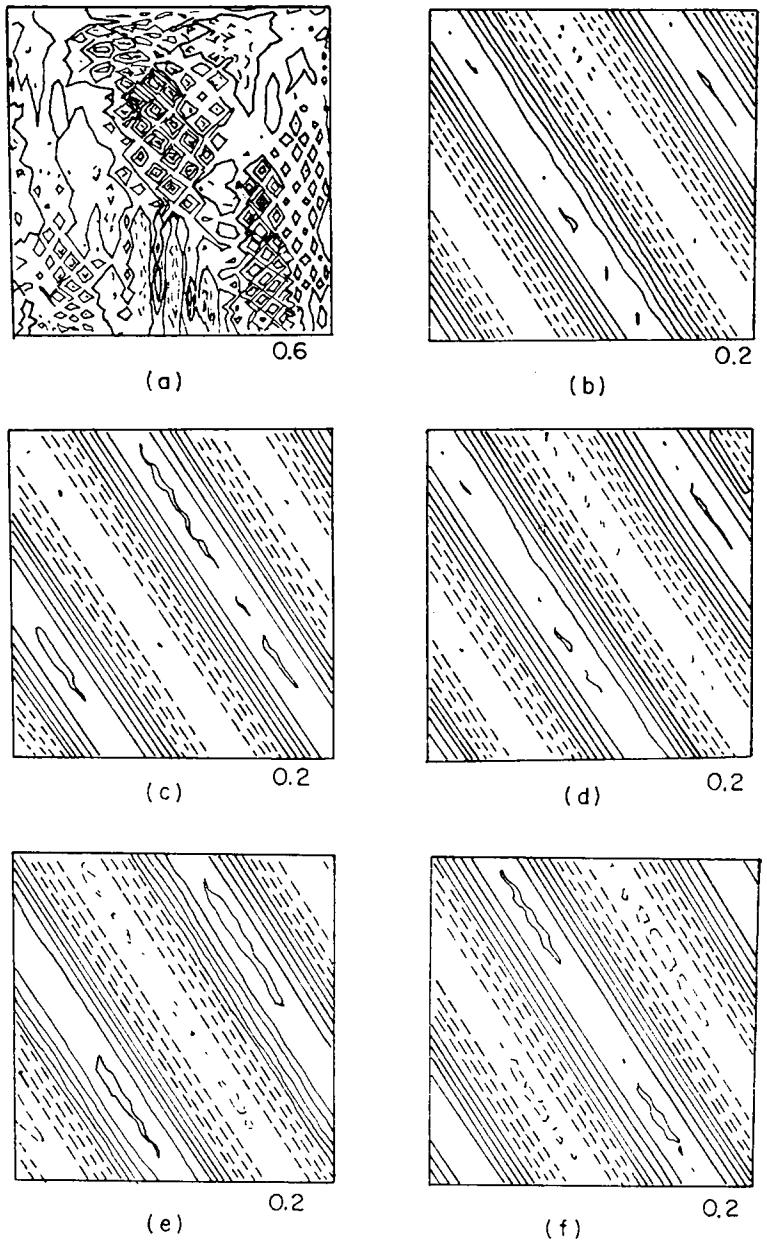

FIG. 13. As Fig. 10. (a, b), (ζ, ψ): PS model, $t = 2.5$ periods, CI = (0.6, 0.2); (c, d), (ζ, ψ): PS model, $t = 2.5$ periods, filtered, CI = (0.2, 0.2); (e, f), (ζ, ψ): PS model, $t = 5.0$ periods, filtered, CI = (0.2, 0.2).

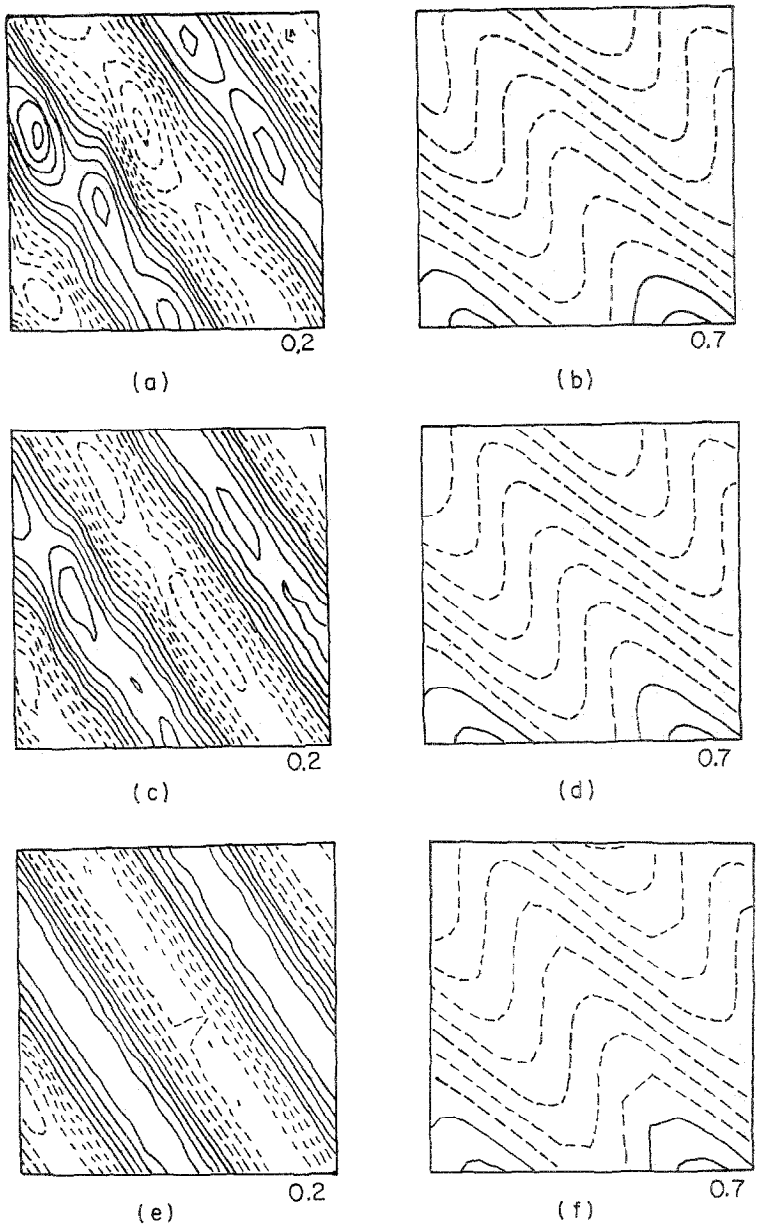

FIG. 14. Nonlinear Rossby waves with $(\nu, \eta, k, l, \epsilon, \gamma) = (32/3.5, 64, 3/13^{1/2}, 2/13^{1/2}, 0.4, 0.5)$. (a, b), (ζ, ψ): FD model, $t = 5$ periods, CI = (0.2, 0.7); (c, d), (ζ, ψ): FF model, $t = 5$ periods, CI = (0.2, 0.7); (e, f), (ζ, ψ): PS model, $t = 5$ periods, CI = (0.2, 0.7), filtered.

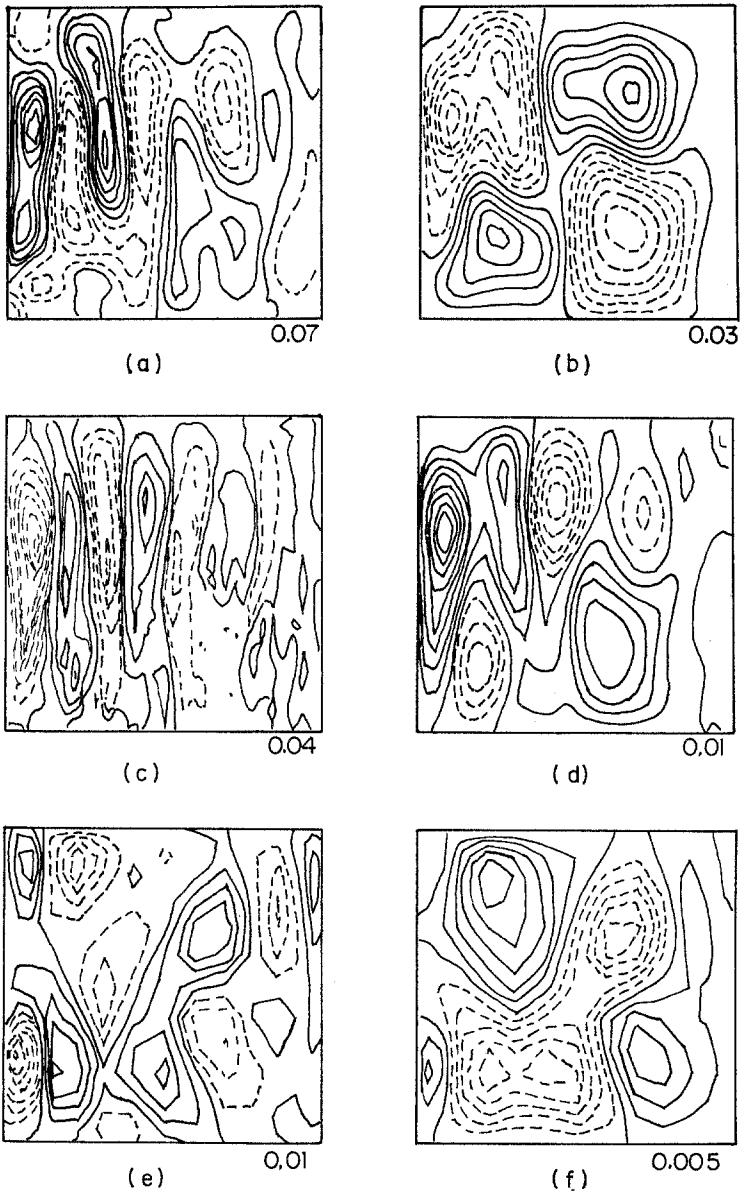

FIG. 15. As Fig. 14. (a, b), (ζ', ψ'): FD model, $t = 5$ periods, CI = (0.07, 0.03); (c, d), (ζ', ψ'): FE model, $t = 5$ periods, CI = (0.04, 0.01); (e, f), (ζ', ψ'): PS model, $t = 5$ periods, CI = (0.01, 5.0×10^{-3}), filtered.

point. This is undoubtedly due to the nature of the spectral expansion which ties points together in just such a manner. The ultimate origin of the PS instability is not known. The site of the instability, for instance, is random and not simply related to the imposed patterns of inflow/outflow along the domain margins.

It has been discovered empirically, however, that periodic spectral filtering effectively controls the generation and accumulation of grid-scale vorticity, and prevents numerical instability in these nonlinear Rossby wave experiments. Figure 13 shows the effect on one such pivotal calculation. By $t = 1.5$ periods, ζ is entirley dominated by two regions of high-wavenumber noise in the unfiltered calculation. When the simulation is redone with filtering, however, the Rossby wave is easily advanced in time to $t = 5$ periods. The final field is quite free of grid-scale noise (Figs. 10e,f and 14e,f).

Filtering of this kind stabilizes a wide range of nonlinear Rossby wave calculations

rable FD test and somewhat smaller than those given by the FE model. RMS(ψ') and RMS(ζ') grow linearly in time [perhaps with some initially large value of the errors due to the filtering] (Figs. 12 and 16). There is very little accumulation of unresolvable features in the vorticity field (Figs. 10e,f and 14e,f). The removal of these small-scale features by filtering does not, however, seem to have a strong effect on the energy of the system.

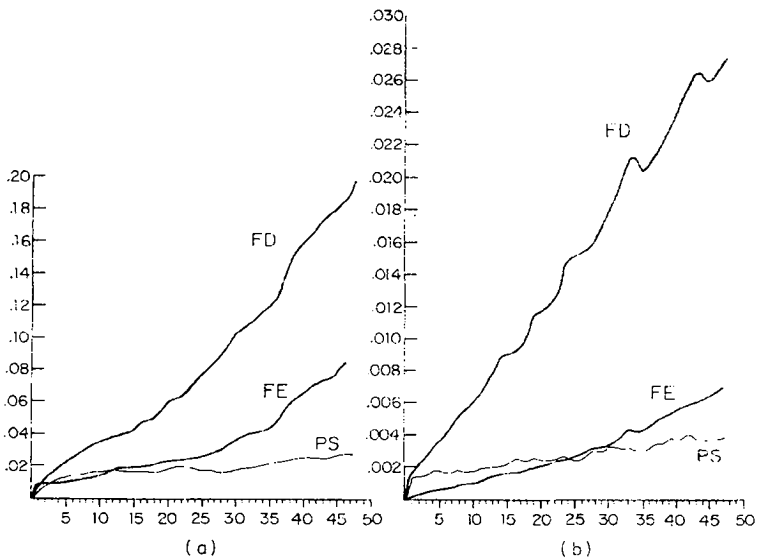

FIG. 16. As Fig. 14, $0 \leqslant t \leqslant 5$ periods. (a, b), RMS(ζ', ψ'): FD model; FE model; PS model, filtered.

6.5. *Intercomparison*

The parametric results of the linear Rossby wave calculations confirm the conclusions of Section 4.5 in which it was noted that the FE and PS models were in general more accurate than the FD code, except for certain optimal choices of the computational parameters ν and η. In addition, the orientation of the Rossby wave has a strong influence on the RMS errors of the FD model. All three models are stable for $\epsilon = 0$.

When nonlinearity is admitted, however, the finite-difference and finite-element models are alone capable of delivering stable and accurate calculations of moderate duration ($t \leqslant 5$ periods) over a broad range of parameters. The spectral model is typically unstable in these instances unless it is supplemented by periodic spectral filtering of the vorticity field.

As a preliminary test of the response of the finite-difference and finite-element models to the addition of a scale-selective vorticity filtering mechanism, we have redone FD and FE experiments 16, 17, and 19 and FE experiment 7 with the application at each time step of a 16th-order Shapiro filter [35]. The results of these comparisons indicate that the RMS errors of the FE calculations are generally lowered somewhat by the addition of filtering (particularly RMS(ζ'), whose smaller scale components are being eliminated by the filtering) and its instabilities delayed (but not removed). The opposite, namely an increase of error with the application of filtering, is often true of the FD simulations. It is not obvious why this should be the case unless the computational boundary condition used in the FD formulation interacts in some systematic way with the applied filtering.

It is of interest to note, however, that all three models (perhaps with some distribution of wavenumber selective filtering) can be made to yield accurate solutions to these open domain problems. In fact, the models have error accumulation characteristics not greatly different than those noted in closed-basin problems. Specifically, the FE and PS models are many times more accurate for given ν and η than the FD model, with the PS being overall the best. Even taking into account the increased efficiency of the finite-difference scheme (Table II), the difference between the second-order and higher-order methods is significant. It is estimated that the FE ($N = 33$) and PS ($N = 17$) models are, on the average, 4 and 15 times more accurate, respectively, than a FD model with $N \simeq 43$ for which the running times of all three models would be approximately equal.

7. Summary and Conclusion

We have integrated the inviscid barotropic vorticity equation under a variety of assumed initial and boundary conditions corresponding to linear and nonlinear box modes, forced nonlinear box modes, and linear and nonlinear Rossby waves. The former two classes of problems are defined within closed domains; the latter is totally open with respect to a presupposed external environment and therefore represents

prototype limited-area calculations for the ocean. Each problem has been solved using second-order finite-difference, fourth-order finite-element, and infinite-order spectral approximation techniques. For each of the three models a series of calculations was performed to determine its accuracy, stability, and efficiency as functions of problem type and the associated physical and computational nondimensional parameters. The most important of these parameters are ϵ, the Rossby number, and ν and η, nondimensional measures of the spatial and temporal resolutino of the numerical approximation. The accuracy of model results was determined, wherever possible, by comparing to known analytic or reference solutions. RMS measures of the errors in the computed values of vorticity, RMS(ζ'), and streamfunction, RMS(ψ'), and a measure of the gain or loss of globally integrated kinetic energy, NDIF(NRG), were tabulated. Integrations of moderate length (5–10 periods of the reference solution) were performed as an empirical measure of the functional dependence of model stability on the parameters. As a result of these calculations, we are able to make model–model intercomparative statements for a sequence of linear and nonlinear problems in open, as well as closed, domains. To our knowledge, such intercomparisons have not previously been made. A more lengthy summary of the parameters and error norms can be found in Section 2. A complete discussion of results has been given in Sections 4–6 and Table I.

These tests have shown that all three models are capable of delivering efficient long-term solutions of acceptable accuracy to linear and weakly nonlinear problems in both closed and open domains. The results also suggest that given a judicious selection of frictional (filtering) mechanism and/or computational boundary condition, each of the models can be made comparably accurate for highly nonlinear calculations. (This hypothesis is being tested in a related series of experiments.) We conclude, therefore, that any of the physical/numerical models investigated here – modified perhaps by additional dissipative or boundary condition assumptions – could be used for the limited-area modeling applications mentioned in the Introduction.

Under the assumption of inviscid dynamics, the operational performance of the three models is most sensitively related to the Rossby number, ϵ. For $0 \lesssim \epsilon \lesssim 0.2$, all the models are stable in the long term. Furthermore, unless an optional choice of ν and η, the nondimensional space and time steps, is made, the spectral and finite-element models are the most accurate, and the finite-difference the least. That this ranking reflects the formal spatial accuracies of the models has been demonstrated by a simple phase error analysis for the linear box mode problems – Section 4.2. The net result of this increased accuracy is that, for a given admissable error, both the FE and PS models are many times more efficient than the FD model (Section 6.5). These conclusions are valid independent of problem class.

Although the PS (and to a lesser degree the FE) models are susceptible to eventual numerical instability characterized by the catastrophic accumulation of grid-scale vorticity features, it has been found that stability can often be maintained, and errors reduced, by a periodic filtering (smoothing) procedure. The RMS error norms of the FE (but not always the FD) model are also reduced with the application of a scale-

selective (Shapiro-type) vorticity filter. Related calculations not reported here have validated the use of these higher-order filtering mechanisms over a wide range of problems. The important point here is that even relatively ad hoc removal of small-scale vorticity prolongs the useful length of integration and increases the accuracy of highly nonlinear simulations.

Lastly, we reiterate the fact that these test calculations do not provide—and were not intended to provide—a definitive comparison of finite-difference, finite-element, and spectral approximation techniques per se. (A fourth-order finite-difference model, for instance, would have fared much better against the finite-element code.) What they do tell us, and what was not known beforehand, is that all three numerical procedures can be made to yield stable and accurate solutions to these idealized open ocean problems. More importantly, the FD, FE, and PS techniques appear to retain their relative formal accuracies in spite of the much more formidable physical and numerical problem that these limited-area calculations represent.

Appendix I

Implementation of the Sundstrom/Davies Boundary Condition

Consider a region near the boundary with the following local ordering.

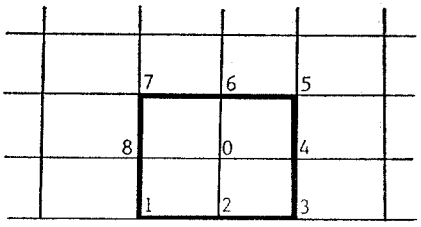

The vorticity equation applied at point 0 will involve vorticity values on the other eight numbered points.

$$\zeta_0^{k+1} - \zeta_0^{k-1} = -\frac{\Delta t}{\Delta x}(\psi_4^{\,k} - \psi_8^{\,k}) - Q\sum_{r=1}^{8} J_r \zeta_r^{\,k}, \tag{A1}$$

where $Q = \epsilon \Delta t/h^2$ and J_r is the Arakawa Jacobian term for the rth point evaluated at point 0.

The Sundstrom/Davies closure for boundary point 2 is

$$\zeta_0^{k+1} + \zeta_0^{k-1} = \zeta_2^{\,k} + \zeta_6^{\,k}. \tag{A2}$$

ζ_0^{k+1} can be eliminated from (A1) and (A2) and the result can be written:

$$QJ_1\zeta_1^{\,k} + (1 + QJ_2)\,\zeta_2^{\,k} + QJ_3\zeta_3^{\,x} = R_2\,, \tag{A3}$$

where

$$R_2 = 2\zeta_0^{k-1} - \zeta_6^{k} - \frac{\Delta t}{h}(\psi_4^{k} - \psi_8^{k}) - Q\sum_{r=4}^{8} J_r\zeta_r^{k}. \tag{A4}$$

In this numerical procedure, the interior vorticity and streamfunction are computed before the boundary vorticity. Equation (A3) is arranged so that R_2 contains only known quantities. For each point along a boundary (but not at corners), (A3) applies.

Were it not for corner points, the system of Eq. (A3) would be of tridiagonal form and easily invertible. Consider a region near the (southeast) corner

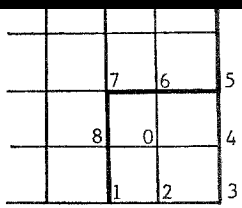

For the boundary condition at the corner, we take the spatial average along the diagonal

$$\zeta_0^{k+1} + \zeta_0^{k-1} = \zeta_3^{k} + \zeta_7^{k}. \tag{A5}$$

It would seem that near corners a pentadiagonal system is required since the Jacobian evaluated at 0 involves the five unknown boundary values at points 1 through 5. However, the Sundstrom/Davies conditions at points 2 and 4 are

$$\zeta_0^{k+1} + \zeta_0^{k-1} = \zeta_2^{k} + \zeta_6^{k} \tag{A6}$$

and

$$\zeta_0^{k+1} + \zeta_0^{k-1} = \zeta_3^{k} + \zeta_7^{k}. \tag{A7}$$

Thus,

$$\zeta_2^{k} = \zeta_3^{k} + \zeta_7^{k} - \zeta_6^{x} \tag{A8}$$

and

$$\zeta_4^{x} = \zeta_3^{x} + \zeta_7^{x} - \zeta_8^{x}. \tag{A9}$$

This means that boundary points which are corner neighbors can be expressed in terms of the corner vorticity and known values. Equations (A8) and (A9) are applied in conjunction with the equations requiring vorticity values of the corner neighbor, i.e., the corner and the two boundary points $2h$ from the corner.

The unknowns in the tridiagonal system are given a cyclic ordering excluding the corner neighbor points.

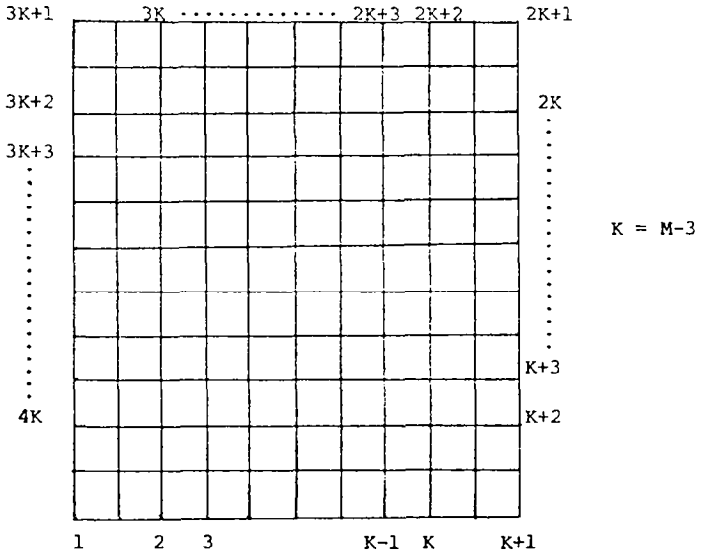

In the diagram the ordering is started in the southwest corner, and (A3) is a tridiagonal system with cyclic boundary conditions since points 1 and $4K$ are connected. By a reordering of the points, the tridiagonal cyclic system can be transformed into a pentadiagonal system which requires twice the computation time of a tridiagonal system.

At inflow points, the vorticity is known and (A3) is replaced by

$$\zeta_2{}^k = \zeta_B{}^k, \tag{A10}$$

where $\zeta_B{}^k$ is the specified value. If the origin of the ordering (the southwest corner in the diagram) were inflow, the off-tridiagonal terms expressing the cyclic nature vanish and we are left with a simple tridiagonal system. If the southwest corner is not inflow, renumber the boundary point

$$i' = (i + L - 1) \bmod(4K) + 1,$$

where L is an inflow point. Finally, the values at the eight corner neighbor points are obtained from (A8) and (A9), or specified if inflow.

Acknowledgments

This research was supported by a contract from the Office of Naval Research (N00014-75-C-0225) and a grant from the National Science Foundation (NSF-OCE76-00869) to Harvard University. The computations were performed at the National Center for Atmospheric Research, which is also supported by the National Science Foundation. This paper is contribution No. 115 from the Mid-Ocean Dynamics Experiment.

REFERENCES

1. A. R. ROBINSON, *in* "Science, Technology and the Modern Navy," ONR-37, Office of Naval Research, Arlington, Va., 1976.
2. R. C. KOLLMEYER, "Labrador Current Predictive Model," Ph. D. Thesis, University of Connecticut, 1975.
3. H. E. HURLBERT AND J. D. THOMPSON, *J. Phys. Ocean.* **3** (1973), 16–32.
4. I. ORLANSKI AND M. D. COX, *Geophys. Fluid Dyn.* **4** (1973), 297–332.
5. A. R. ROBINSON, D. E. HARRISON, AND D. B. HAIDVOGEL, *Dyn. Atm. Oceans* **5** (1979), 2–4.
6. MODE Group, *Deep-Sea Res.* **25** (1977), 859–910.
7. J. C. MCWILLIAMS, *J. Phys. Ocean.* **6** (1976), 810–846.
8. C. C. EBBESMEYER, B. A. TAFT, J. COX, J. C. MCWILLIAMS, W. B. OWENS, M. SAYLES, AND C. SHEN, *Polymode News* **54** (1978) (unpublished manuscript).
9. R. LEGECKIS, *Geophys. Res. Lett.* **2** (1975), 435–438.
10. D. E. HARRISON AND A. R. ROBINSON, *Dyn. Atm. Oceans* **2** (1978), 185–211.
11. P. B. RHINES, *in* "The Sea," Vol. 6, "Marine Modeling" (E. D. Goldberg, I. N. McCane, J. J. O'Brien, and J. H. Steele, Eds.), Wiley, New York, 1977.
12. W. B. OWENS AND F. P. BRETHERTON, *Deep-Sea Res.* **25** (1978), 1–14.
13. J. OLIGER AND A. SUNDSTRON, *SIAM J. App. Math.* **35** (1978), 419–446.
14. J. G. CHARNEY, R. FJORTOFT, AND J. VON NEUMANN, *Tellus* **2** (1950), 237–254.
15. A. SUNDSTROM, *Mon. Weather Rev.* **97** (1969), 340–345.
16. A. F. BENNET AND P. E. KLOEDEN, *J. Atm. Sci.* **35** (1978), 990–996.
17. H. C. DAVIES, *J. Comput. Phys.* **13** (1973), 398–422.
18. I. ORLANSKI, *J. Comput. Phys.* **21** (1976), 251–269.
19. A. L. CAMERLENGO AND J. J. O'BRIEN, Open boundary conditions in rotating fluids, submitted for publication.
20. A. F. BENNET, *J. Atm. Sci.* **33** (1976), 176–182.
21. M. A. SHAPIRO AND J. J. O'BRIEN, *J. Appl. Meteorol.* **9** (1970), 345–349.
22. S. A. ORSZAG AND M. ISRAELI, *Ann. Rev. Fluid Mech.* **6** (1974), 281–318.
23. D. B. HAIDVOGEL AND A. R. ROBINSON, *Ocean Modelling* **18** (1978), (unpublished manuscript).
24. A. R. ROBINSON AND D. B. HAIDVOGEL, *Polymode News* **61** (1979), (unpublished manuscript).
25. G. J. FIX, *SIAM J. Appl. Math.* **29** (1975), 371–387.
26. A. ARAKAWA, *J. Comput. Phys.* **1** (1966), 119–143.
27. D. C. JESPERSEN, *J. Comput. Phys.* **16** (1974), 383–390.
28. V. PEREYRA, *SIAM J. Numer. Anal.* **4** (1967), 508–533.
29. D. B. HAIDVOGEL, *in* "Proceedings of the ASME Symposium on Computing Methods in Geophysical Mechanics," ADM Vol. 25, Amer. Soc. Mechanical Engineers, 1977.
30. C. LANCZOS, "Applied Analysis," Prentice–Hall, Englewood Cliffs, N. J., 1956.
31. D. B. HAIDVOGEL AND T. ZANG, The accurate solution of Poisson's equation by expansion in Chebyshev polynomials, in press.
32. S. A. ORSZAG, *Stud. Appl. Math.* **51** (1942), 253–259.
33. J. PEDLOSKY, *Tellus* **19** (1967), 250–256.
34. A. E. GILL, *Geophys. Fluid Dyn.* **6** (1974), 29–47.
35. R. SHAPIRO, *J. Atm. Sci.* **28** (1971), 523–531.